Visceral organ morphogenesis via calcium-patterned muscle constrictions

Noah P Mitchell,[1,2] Dillon J Cislo,[2] Suraj Shankar[1,3]
Yuzheng Lin,[2] Boris I Shraiman,[1] Sebastian J Streichan[2,4*]

[1]Kavli Institute for Theoretical Physics, University of California Santa Barbara, Santa Barbara, CA 93106, USA
[2]Department of Physics, University of California Santa Barbara, Santa Barbara, CA 93106, USA
[3]Department of Physics, Harvard University, Cambridge, MA 02138, USA
[4]Biomolecular Science and Engineering, University of California Santa Barbara, Santa Barbara, CA 93106, USA
*E-mail: streicha@ucsb.edu.

Organ architecture is often composed of multiple laminar tissues arranged in concentric layers. During morphogenesis, the initial geometry of visceral organs undergoes a sequence of folding, adopting a complex shape that is vital for function. Genetic signals are known to impact form, yet the dynamic and mechanical interplay of tissue layers giving rise to organs' complex shapes remains elusive. Here, we trace the dynamics and mechanical interactions of a developing visceral organ across tissue layers, from sub-cellular to organ scale *in vivo*. Combining deep tissue light-sheet microscopy for *in toto* live visualization with a novel computational framework for multilayer analysis of evolving complex shapes, we find a dynamic mechanism for organ folding using the embryonic midgut of *Drosophila* as a model visceral organ. Hox genes, known

regulators of organ shape, control the emergence of high-frequency calcium pulses. Spatiotemporally patterned calcium pulses trigger muscle contractions via myosin light chain kinase. Muscle contractions, in turn, induce cell shape change in the adjacent tissue layer. This cell shape change collectively drives a convergent extension pattern. Through tissue incompressibility and initial organ geometry, this in-plane shape change is linked to out-of-plane organ folding. Our analysis follows tissue dynamics during organ shape change *in vivo*, tracing organ-scale folding to a high-frequency molecular mechanism. These findings offer a mechanical route for gene expression to induce organ shape change: genetic patterning in one layer triggers a physical process in the adjacent layer – revealing post-translational mechanisms that govern shape change.

Introduction

Visceral organ morphogenesis proceeds by the assembly of layered cell sheets into tubes, which develop into complex shapes [1]. Through this process, genetic patterning instructs cellular behaviors, which in turn direct deformations in interacting tissue layers to sculpt organ-scale shape. This motif arises, for instance, in the coiled chambers of the heart, contortions of the gut tube, and branching airways of the lung [2, 3, 4]. Meanwhile, elastic bilayer sheets highlight the potential for mechanical interactions alone to generate nontrivial 3D shape transformations [5]. While studies of monolayer tissue development in planar geometries imaged near the embryo surface or *ex vivo* have uncovered general principles [6, 7, 8, 9], following the dynamics of fully 3D visceral organ shape change has remained out of reach [4, 10]. Physical models inferred from static snapshots of organ morphology have proven useful in this regard, but connecting dynamics at the cellular and sub-cellular level with the dynamics of shape change at the organ

scale through live imaging remains a new frontier [11, 2, 12].

Uncovering cell and tissue dynamics in a shape-shifting organ presents several challenges. A conceptual challenge is that visceral organs exhibit both genetic and mechanical interactions between multiple tissue layers [13, 14]. Technical challenges arise as well, since their complex, dynamic shapes develop deep inside embryos. Capturing dynamics *in vivo* therefore requires imaging methods that overcome image degradation due to scatter [15] and a computational framework for analysis of complex shapes.

The embryonic midgut – composed of muscle cells ensheathing an endodermal layer, linked by extracellular matrix (Fig. 1A) – offers a system in which we can overcome these challenges and probe *in toto* organ dynamics across tissue layers at sub-cellular resolution. Its size and the molecular toolkit of the model system render the midgut ideal for light-sheet microscopy [16], tissue cartography [17], and non-neuronal optogenetics [18]. Hox genes expressed in the muscle layer are required for the midgut to form its four chambers, but the mechanism by which genetic expression patterns are translated into tissue deformation, and in turn to organ shape, remains unclear (Fig. 1B-C) [19, 20, 21, 22, 23, 24, 25]. Here we connect this genetic patterning to mechanical interactions between layers during development and track the kinematic mechanism linking mechanical action to organ shape transformations. We find that dynamic, high-frequency calcium pulses drive patterned muscle contraction, inducing bending and convergent extension in the endoderm to sculpt stereotyped folds.

Results

Live deep tissue imaging reveals bilayer morphogenesis

The midgut is a closed tube by stage 15 of embryonic development, residing 20-60μm below the embryo surface [26]. The organ first constricts halfway along its length, then constricts again to subdivide into four chambers (Video 1). Within $75 - 90$ minutes after the onset of the

first fold, the constrictions are fully formed, and the organ beings to adopt a contorted shape.

Quantitative characterization of these dynamics requires extraction of the full organ's geometry, which is challenging due to tissue scatter. We overcome this challenge by *in toto* live imaging using confocal multi-view light sheet microscopy [15]. In conjunction, we express tissue-specific markers using the GAL4-UAS system [27] in *klarsicht* embryos [28], which exhibit genetically-induced optical clearing (see Methods). To translate this volumetric data into dynamics of the midgut surface, we combine machine learning [29] with computer vision techniques [30, 31] using an analysis package dubbed 'TubULAR' [32]. In this way, we are able to resolve sub-cellular structures with 1 minute temporal resolution (Fig. 1D and fig. S1-4, Video 2).

We find that gut morphogenesis is stereotyped and exhibits reproducible stages (Fig. 1E). The surface area grows by $\sim 30\%$ during folding (stages 15a-16a) and remains constant by the time constrictions are fully formed (16b), despite continued shape change. The enclosed volume within the midgut decreases only gradually during this process, while the effective length of the organ – the length along its curving centerline – triples (Fig. 1E, Methods).

Endodermal cell shape change underlies tissue shape change

How does this 3D shape change occur at the tissue and cellular scale? We first analyzed the endoderm layer. Inspection of these cells reveals strikingly anisotropic cell shapes before constrictions begin (Fig. 1F and Fig. 2A-B). In order to quantify cell shape on this dynamic surface, we cartographically project into the plane using TubULAR [32, 33]. This projection preserves defines a global coordinate system in which we unambiguously define the anterior-posterior (AP) and circumferential axes for all time points, even when the organ exhibits deep folds and contortions (Fig. 2 - supplement 1 and [32]).

By segmenting cell shapes, we find that endodermal cells are strongly anisotropic, with an

average aspect ratio $a/b > 2$, and are globally aligned along the circumferential axis (Fig. 2A-C). As constrictions develop, cells loose this anisotropy and even become elongated along the AP axis in posterior regions (Fig. 2B-C and Fig. 2 - supplement 2A). Measurement of endodermal cell orientations reveal that this effect is not due to rotations (Fig. 2D). As shown in Fig. 2 - supplement 2A, the initial anisotropy is patterned along the AP axis so that cells near two of the constriction locations are most anisotropic. While we do not presently know the mechanism of this patterning, it suggests these tissue regions may be primed for deformation by positional information before constrictions begin. Subsequent cell shape change is greatest near each constriction, as shown in Fig. 2 - supplement 2B.

Despite the large changes in aspect ratio, cell areas in the endoderm change only gradually (Fig. 2E), such that cells converge along the circumferential axis while extending along the folding longitudinal axis. On a larger scale, the observed cellular deformation would collectively generate tissue movement called convergent extension. At the same time, other processes – such as oriented divisions or cell intercalations – could also contribute or counteract tissue-scale convergent extension [34]. However, we find no signs of cell division during this process, confirming previous observations [26]. Moreover, though tracking quartets of cells in the anterior midgut revealed widespread intercalations (also called T1 transitions), the orientations of these events were not significantly biased for the early stages of constriction (Fig. 2 - supplement 3 and Video 3). This suggests that anisotropic cell shape change may be the primary contributor to tissue-scale shape change. We next tested this hypothesis, asking how in-plane, cell-scale shape change connects to out-of-plane, tissue-scale deformations during constrictions.

Tissue-scale convergent extension via constriction

To understand the kinematic mechanism underlying organ shape, we must bridge spatial scales from cell deformation to meso-scale tissue deformation. Given that the midgut tissue is thin

compared to the organ radius, cells exert forces on one another primarily through in-plane interactions, but in-plane mechanical stress can couple to curvature to generate out-of-plane motion [35]. In a nearly incompressible tissue constricting out-of-plane, cells do not change area, but may change shape, collectively driving in-plane motion. In particular, the out-of-plane motion v_n would couple to in-plane motion $\mathbf{v}_\parallel$ through the mean curvature H, such that

$$2Hv_n \approx \nabla \cdot \mathbf{v}_\parallel, \tag{1}$$

where $\nabla \cdot \mathbf{v}_\parallel$ is the in-plane divergence of the tissue motion along the surface. Such a kinematic constraint guides the shape changes that result from prescribed patterns of mechanical stresses in the tissue.

We hypothesized that the constricting midgut may behave as nearly incompressible, given that we found cell areas to vary only gradually during constrictions. To test this, we extract whole-organ tissue deformation patterns and find strong out-of-plane motion and in-plane dilatational flows concentrated near folds (Fig. 2A, Video 4, and Fig. 3 - supplement 1). Remarkably, we find that the pattern of out-of-plane deformation almost entirely accounts for in-plane dilatational motion in the gut, with only a small change in local tissue areas (Video 5). This tight link suggests that the tissue behaves as an incompressible medium. As shown in Fig. 3B, these terms match with 97% correlation, leaving a residual in-plane growth residue at the level of $\sim$1% per minute. This slow residual area growth, which is primarily concentrated in the lobes of rounding gut chambers, accounts for the cellular area growth noted in Fig. 1E and the surface area growth in Fig. 2E.

Because the organ is curved into a tube, constrictions converge the tissue along the circumferential axis, and tissue incompressibility couples inward motion to extension along the longitudinal axis to preserve areas (Fig. 3C). We dub this kinematic mechanism 'convergent extension via constriction': as the tissue constricts with an inward normal velocity, the length

of the tissue along the circumferential direction shortens while curves along the longitudinal (AP) axis of the organ lengthen, keeping the areas of cells approximately constant (Fig. 3D-F and Fig. 3 - supplement 3). As a consequence of tissue incompressibility and localized constrictions, the resulting area-preserving deformations are largest near constrictions (Fig. 3 - supplement 4), mirroring the pattern of cell-scale deformations. Though the shape of the organ becomes increasingly complex, in-plane deformations remain globally aligned in the material coordinate system: the tissue converges and extends along the circumferential and longitudinal axes, respectively, even as these axes deform in 3D space as morphogenesis proceeds (Fig. 3 - supplement 4).

Finally, we find that tissue convergent extension is accounted for primarily by our previous measurement of cell shape change. Since the early stages of midgut constrictions have no divisions or oriented cell intercalations, we hypothesized that cell shape change alone can explain the tissue scale convergent extension. Fig. 3 - supplement 5 shows a quantitative match between cell shape changes and tissue convergent extension, indicating that local cell shape changes primarily mediate tissue-scale convergent extension during the early stages of constrictions. During stage 16b, the tight association between cell-scale and tissue-scale deformations loosens, corresponding to contributions from cell intercalations [36].

In short, we established a link from endodermal cell shape change to tissue-scale folding – in which incompressibility couples out-of-plane deformation to in-plane motion – resulting in convergent extension via constriction (Fig. 3G). What mechanical process drives strong, localized contractions at the folds?

Muscle contractions drive cell and tissue shape change

It is known that embryos with either disrupted muscle or endoderm structure fail to fold [37, 38, 39, 21], as do embryos lacking integrins linking the two layers [40]. This suggests that

gut morphogenesis requires an interaction between muscle and endodermal layers. At the same time, hox genes – which are expressed exclusively in the muscle layer – have been linked to the successful formation of specific folds (Fig. 4A-B) [41]. In particular, *Antp* mutants lack the anterior fold lying near the center of the *Antp* domain (Fig. 4C), while *Ubx* mutants lack the middle fold lying at the posterior edge of the *Ubx* domain (Fig. 4D). In this system, genetic patterning of the endoderm occurs via genetic patterning from the muscle layer [19, 42], so it is possible that constrictions result from a *genetic* induction process. Alternatively, *mechanical* interactions between the layers could induce a program of convergent extension in the endoderm – with patterned deformation of the muscle layer sculpting a passive, tethered endoderm [24] or triggering active endodermal cell shape change.

To clarify the relationship between layers during constriction dynamics, we first measured relative motion of the muscle layer against the endoderm. By tracking both circumferential muscle nuclei and endoderm nuclei in the same embryo, we find that these two layers move together, with initially close nuclei separating by $\sim 5\mu$m per hour (Fig. 4E-F, Videos 6-7, and Methods). This result is consistent with the notion that the two layers are tightly tethered by the integrins and extracellular matrix binding the heterologous layers [40].

Based on this tight coupling, we hypothesized that muscle mechanically induces shape change in the tethered endoderm. To test this hypothesis, we inhibited contractility of the muscle layer by driving *UAS-CIBN UAS-CRY2-OCRL*, a two-component optogenetic construct that recruits *OCRL* to the plasma membrane to dephosphorylate PI(4,5)P_2. This process has been shown to abolish actomyosin contractility in other developmental contexts by releasing actin from the plasma membrane [18]. Driving *CRY2-OCRL* with *Antp-GAL4* under continuous activation of blue light reliably prevented anterior folding (Fig. 4G). Likewise, driving *CIBN* and *CRY2-OCRL* under continuous blue light activation in muscle regions posterior to the anterior fold using *Ubx-GAL4 M1* locally inhibited constriction dynamics. We note that *Ubx-GAL4*

M1 embryos express *Ubx* in a larger domain than the endogenous WT *Ubx* domain due to differences in its regulation [43], but *Ubx-GAL4 M1* embryos nonetheless execute all three constrictions in the absence of *UAS-CRY2-OCRL* under similar imaging conditions. Inhibiting contraction in selected regions therefore mimics the genetic mutants known to remove folds.

Given that muscle contractility is required, we asked if optogenetically inducing actomyosin contraction in the muscle is sufficient to induce constrictions. Indeed, optogenetic activation using the *CIBN UAS-ρGEF2* system in the *Antp* region generates an anterior fold on demand on the timescale of a few minutes, even if induced long before the constriction would normally begin (Fig. 4G). Similarly, activation of the *Ubx-GAL4 M1* domain results in a nearly uniform constriction that dramatically alters the shape of the organ, forcing the yolk to flow into the anterior chamber. Additional optogenetic experiments inhibiting contractility of all muscles likewise led to folding defects ($N = 13$, *w;UAS-CIBN::GFP;Mef2-GAL4/UAS-CRY2-OCRL:mCherry*). We conclude that muscle contractility is necessary for constrictions and inducing contraction and the associated downstream behaviors is sufficient to generate folds.

We then asked how these macro-scale perturbations on organ shape are linked to cell shapes in the endoderm. In contrast with the wild-type, endodermal cell shape changes are significantly reduced under optogenetic inhibition of muscle contractility. As shown in Fig. 4H-I, cell segmentation of the endoderm during optogenetic inhibition of muscle contraction in the *Antp* domain reveals nearly constant aspect ratios: the endoderm cells near the *Antp* domain undergo reduced convergent extension when muscle contraction is locally disrupted (single-sided z-test: $p = 1 \times 10^{-6}$ for difference after 1 hr, $p = 1 \times 10^{-22}$ for sustained difference between curves, see Methods). We also observe analogous reduction of endodermal cell shape change in *Antp* mutants, which lack anterior folds (Fig. 4I, single-sided z-test: $p = 7 \times 10^{-3}$ for difference after 1 hr, $p = 4 \times 10^{-9}$ for sustained difference between curves). Thus, the endodermal program of convergent extension is induced by mechanical interaction with the contracting muscle layer.

Calcium pulses spatiotemporally pattern muscle contractility

What mechanism triggers muscle contractions, allowing such sharp folds to arise? Recent studies have shown that calcium signaling triggers muscle contractions in a wide range of contexts [44]. If hox genes use calcium signaling to pattern muscle contraction in the midgut, we would predict that calcium pulses appear near localized constrictions. Furthermore, hox gene mutants lacking folds would not exhibit localized calcium pulses, and inhibition of the cell biological mechanism translating calcium into mechanical contraction should likewise inhibit constrictions.

To test for a link from hox genes to organ shape through this mechanism, we fist imaged a fluorescent probe of calcium dynamics (*GCaMP6s*) in the muscle layer. As shown in Fig. 5A-E and Video 8, dynamic calcium pulses appear in the muscle layer in regions localized near all three midgut constrictions. Additionally, these calcium pulses are patterned in time, appearing only at the onset of constriction for each fold (fig. S17).

To test whether hox genes pattern shape change through calcium dynamics, we measured *GCaMP6s* activity in flies mutant for *Antp* that lack an anterior constriction. As shown in Fig. 5F, we found that calcium activity was almost entirely absent during stages 15-16. Calcium activity is strongly reduced at the location of the missing anterior constriction (single-sided z-test: $p = 2 \times 10^{-8}$) and subsequent calcium pulses are repressed within the vicinity of the region for the hour after the constriction would normally initiate (single-sided z-test: $p = 1 \times 10^{-13}$ within 50 μm, Video 9 and Fig. 5 - supplement 3). The hox gene *Antp* is therefore upstream of dynamic calcium pulses.

Importantly, we also find that in wild-type embryos, knock-downs of calcium signaling remove folds. In smooth muscle cells, calcium is known to trigger muscle contraction by binding to calmodulin, which in turn binds to myosin light chain kinase (MLCK) to trigger myosin light chain phosphorylation [45], and cytoplasmic calcium is transported from the cytosol into

the sarcoplasmic reticulum for storage under regulation of SERCA [44]. Driving a dominant negative form of SERCA previously shown to exhibit temperature-sensitive expression under *Mef2-GAL4* [46], we find that disrupting calcium signaling via heatshock beginning at stages 13-15a suppressed midgut constrictions ($p = 7 \times 10^{-9}$, Fig. 5G, Video 10). Separately, interrupting the production of MLCK in the muscle via RNA interference demonstrates a similar reduction in folding behavior ($p = 2 \times 10^{-4}$, Fig. 5G). From this we infer that spatially localized calcium dynamics – under the control of hox gene patterning – triggers MLCK signaling leading to muscle contractions (Fig. 5H).

Discussion

Here we studied morphogenesis of an organ in which heterologous tissue layers generate complex shape transformations. We found that convergent extension and sharp folds in the endodermal layer are triggered by mechanical interaction of muscle contractility together with tissue incompressibility, and patterns of calcium signaling regulate contractility in muscle cells according to hox-specified information (Fig. 5H).

Though correspondences between hox genes and cell fates have been established for decades [26], understanding the physical processes driven by hox genes remains an active area of research. Here we demonstrated a link from genes to tissue morphodynamics through active forces, connecting hox genes to a mechanical induction cascade across layers that integrates high frequency calcium pulses to advance reproducible morphogenesis of complex 3D shape. While calcium dynamics have known roles in early developmental stages of diverse organisms [47, 48, 49, 50] – including influencing the organization of muscle fibers in the midgut [14] and determining cell fates in heart valves [51] – our findings suggest a direct influence of calcium on shape, wherein pulses trigger a program of irreversible tissue deformation. These calcium-patterned muscle contractions control 3D shape through a mechanical cascade across tissue layers, with

broad relevance to tissue engineering and organ morphogenesis in other organisms.

At the cellular level, a remaining question is how the midgut selects precise positions and times for localized calcium activity despite broad hox gene domains that vary slowly with time. For example, the anterior fold forms near the center of the *Antp* domain. Do cells sense subtle gradients of *Antp*, or does more refined patterning downstream of hox gene expression specify this location [52]? One available avenue for the latter possibility is that hox genes govern the formation of anatomical structures that may transmit signals from the soma to trigger calcium pulses [53].

At the tissue level, a remaining question is to what extent endodermal cells actively respond to muscle contraction, rather than passively deforming. For instance, there could be a mechanical signaling pathway provoking contractile behavior in endodermal cells, or even a mechanical induction loop between layers regulating morphological progression. Our findings open new avenues to study how dynamic interactions between layers encode complex shapes of visceral organs.

Acknowledgments

This research was supported by NIH Grant No. R35 GM138203 and NIH Grant No. R00 HD088708, and was supported in part by the National Science Foundation Grant No. NSF PHY-1748958. We thank members of the Streichan and Shraiman labs, Eric Wieschaus, and Zvonimir Dogic for valuable insights, discussions, and suggestions. Isaac Breinyn aided in early exploration of the system. Matt Lefebvre, Isaac Breinyn, and Sophie Streichan aided in handling several stocks, crosses, and reagents. We acknowledge Ben Lopez in the NRI-MCDB Microscopy Facility for support and maintenance of the Resonant Scanning Confocal supported by the NSF MRI grant DBI-1625770. The authors acknowledge the use of the Microfluidics Laboratory (Innovation Workshop) within the California NanoSystems Institute, supported by

the University of California, Santa Barbara and the University of California, Office of the President. NPM acknowledges support from the Helen Hay Whitney Foundation. SS acknowledges support from the Harvard Society of Fellows.

References

[1] Nelson, C. M. & Gleghorn, J. P. Sculpting Organs: Mechanical Regulation of Tissue Development. *Annual Review of Biomedical Engineering* **14**, 129–154 (2012).

[2] Savin, T. *et al.* On the growth and form of the gut. *Nature* **476**, 57–62 (2011).

[3] Le Garrec, J.-F. *et al.* A predictive model of asymmetric morphogenesis from 3D reconstructions of mouse heart looping dynamics. *eLife* **6**, e28951 (2017).

[4] Metzger, R. J., Klein, O. D., Martin, G. R. & Krasnow, M. A. The branching programme of mouse lung development. *Nature* **453**, 745–750 (2008).

[5] van Rees, W. M., Vouga, E. & Mahadevan, L. Growth patterns for shape-shifting elastic bilayers. *Proceedings of the National Academy of Sciences* **114**, 11597–11602 (2017).

[6] Irvine, K. & Wieschaus, E. Cell intercalation during Drosophila germband extension and its regulation by pair-rule segmentation genes. *Development* **120**, 827–841 (1994).

[7] Streichan, S. J., Lefebvre, M. F., Noll, N., Wieschaus, E. F. & Shraiman, B. I. Global morphogenetic flow is accurately predicted by the spatial distribution of myosin motors. *eLife* **7**, e27454 (2018).

[8] Saadaoui, M., Rocancourt, D., Roussel, J., Corson, F. & Gros, J. A tensile ring drives tissue flows to shape the gastrulating amniote embryo. *Science* **367**, 453–458 (2020).

[9] Rauskolb, C., Sun, S., Sun, G., Pan, Y. & Irvine, K. D. Cytoskeletal Tension Inhibits Hippo Signaling through an Ajuba-Warts Complex. *Cell* **158**, 143–156 (2014).

[10] Pérez-González, C. *et al.* Mechanical compartmentalization of the intestinal organoid enables crypt folding and collective cell migration. *Nature Cell Biology* **23**, 745–757 (2021).

[11] Vignes, H. *et al.* Extracellular mechanical forces drive endocardial cell volume decrease during zebrafish cardiac valve morphogenesis. *Developmental Cell* **57**, 598–609.e5 (2022).

[12] Shyer, A. E. *et al.* Villification: How the Gut Gets Its Villi. *Science* **342**, 212–218 (2013).

[13] Sivakumar, A. & Kurpios, N. A. Transcriptional regulation of cell shape during organ morphogenesis. *Journal of Cell Biology* **217**, 2987–3005 (2018).

[14] Huycke, T. R. *et al.* Genetic and Mechanical Regulation of Intestinal Smooth Muscle Development. *Cell* **179**, 90–105.e21 (2019).

[15] de Medeiros, G. *et al.* Confocal multiview light-sheet microscopy. *Nature Communications* **6**, 8881 (2015).

[16] Krzic, U., Gunther, S., Saunders, T. E., Streichan, S. J. & Hufnagel, L. Multiview light-sheet microscope for rapid in toto imaging. *Nature Methods* **9**, 730–733 (2012).

[17] Heemskerk, I. & Streichan, S. J. Tissue Cartography: Compressing Bio-Image Data by Dimensional Reduction. *Nature methods* **12**, 1139–1142 (2015).

[18] Guglielmi, G., Barry, J. D., Huber, W. & De Renzis, S. An Optogenetic Method to Modulate Cell Contractility during Tissue Morphogenesis. *Developmental Cell* **35**, 646–660 (2015).

316 [19] Bienz, M. Induction of the endoderm in Drosophila. *Seminars in Cell & Developmental*
317 *Biology* **7**, 113–119 (1996).

318 [20] Hoppler, S. & Bienz, M. Specification of a single cell type by a Drosophila homeotic
319 gene. *Cell* **76**, 689–702 (1994).

320 [21] Wolfstetter, G. *et al.* Fusion of circular and longitudinal muscles in Drosophila is indepen-
321 dent of the endoderm but further visceral muscle differentiation requires a close contact
322 between mesoderm and endoderm. *Mechanisms of Development* **126**, 721–736 (2009).

323 [22] Bienz, M. & Tremml, G. Domain of Ultrabithorax expression in Drosophila visceral
324 mesoderm from autoregulation and exclusion. *Nature* **333**, 576–578 (1988).

325 [23] Immerglück, K., Lawrence, P. A. & Bienz, M. Induction across germ layers in Drosophila
326 mediated by a genetic cascade. *Cell* **62**, 261–268 (1990).

327 [24] Reuter, R. & Scott, M. Expression and function of the homoeotic genes Antennapedia and
328 Sex combs reduced in the embryonic midgut of Drosophila. *Development* **109**, 289–303
329 (1990).

330 [25] Panganiban, G., Reuter, R., Scott, M. & Hoffmann, F. A Drosophila growth factor ho-
331 molog, decapentaplegic, regulates homeotic gene expression within and across germ lay-
332 ers during midgut morphogenesis. *Development* **110**, 1041–1050 (1990).

333 [26] Bate, M. & Martinez Arias, A. (eds.) *The Development of Drosophila melanogaster* (Cold
334 Spring Harbor Laboratory Press, 1993).

335 [27] Brand, A. & Perrimon, N. Targeted gene expression as a means of altering cell fates and
336 generating dominant phenotypes. *Development* **118**, 401–415 (1993).

[28] Welte, M. A., Gross, S. P., Postner, M., Block, S. M. & Wieschaus, E. F. Developmental Regulation of Vesicle Transport in Drosophila Embryos: Forces and Kinetics. *Cell* **92**, 547–557 (1998).

[29] Berg, S. *et al.* ilastik: interactive machine learning for (bio)image analysis. *Nature Methods* **16**, 1226–1232 (2019).

[30] Márquez-Neila, P., Baumela, L. & Alvarez, L. A Morphological Approach to Curvature-Based Evolution of Curves and Surfaces. *IEEE Transactions on Pattern Analysis and Machine Intelligence* **36**, 2–17 (2014).

[31] Chan, T. & Vese, L. Active contours without edges. *IEEE Transactions on Image Processing* **10**, 266–277 (2001).

[32] Mitchell, N. P. & Cislo, D. J. Tubular: Tracking deformations of dynamic tissues and interfaces in 3d. *bioRxiv* (2022). 10.1101/2022.04.19.488840.

[33] Aigerman, N. & Lipman, Y. Orbifold Tutte embeddings. *ACM Transactions on Graphics* **34**, 190:1–190:12 (2015).

[34] Etournay, R. *et al.* Interplay of cell dynamics and epithelial tension during morphogenesis of the Drosophila pupal wing. *eLife* **4**, e07090 (2015).

[35] Arroyo, M. & DeSimone, A. Relaxation dynamics of fluid membranes. *Physical Review E* **79**, 031915 (2009).

[36] Blanchard, G. B. *et al.* Tissue tectonics: morphogenetic strain rates, cell shape change and intercalation. *Nature Methods* **6**, 458–464 (2009).

[37] Bilder, D. & Scott, M. P. Genomic Regions Required for Morphogenesis of the Drosophila Embryonic Midgut. *Genetics* **141**, 1087–1100 (1995).

[38] Wolfstetter, G. *et al.* The scaffolding protein Cnk binds to the receptor tyrosine kinase Alk to promote visceral founder cell specification in Drosophila. *Science Signaling* **10** (2017).

[39] Singer, J. B., Harbecke, R., Kusch, T., Reuter, R. & Lengyel, J. A. Drosophila brachyenteron regulates gene activity and morphogenesis in the gut. *Development* **122**, 3707–3718 (1996).

[40] Devenport, D. & Brown, N. H. Morphogenesis in the absence of integrins: mutation of both Drosophila Beta subunits prevents midgut migration. *Development* **131**, 5405–5415 (2004).

[41] Tremml, G. & Bienz, M. Homeotic gene expression in the visceral mesoderm of Drosophila embryos. *The EMBO Journal* **8**, 2677–2685 (1989).

[42] Mendoza-Garcia, P. *et al.* DamID transcriptional profiling identifies the Snail/Scratch transcription factor Kahuli as an Alk target in the Drosophila visceral mesoderm. *Development* **148**, dev199465 (2021).

[43] Garaulet, D. L., Foronda, D., Calleja, M. & Sánchez-Herrero, E. Polycomb-dependent Ultrabithorax Hox gene silencing induced by high Ultrabithorax levels in Drosophila. *Development* **135**, 3219–3228 (2008).

[44] Kuo, I. Y. & Ehrlich, B. E. Signaling in Muscle Contraction. *Cold Spring Harbor Perspectives in Biology* **7**, a006023 (2015).

[45] Hill-Eubanks, D. C., Werner, M. E., Heppner, T. J. & Nelson, M. T. Calcium Signaling in Smooth Muscle. *Cold Spring Harbor Perspectives in Biology* **3**, a004549 (2011).

[46] Kaneko, M., Desai, B. S. & Cook, B. Ionic leakage underlies a gain-of-function effect of dominant disease mutations affecting diverse p-type atpases. *Nature Genetics* **46**, 144–151 (2014).

[47] Wallingford, J. B., Ewald, A. J., Harland, R. M. & Fraser, S. E. Calcium signaling during convergent extension in Xenopus. *Current Biology* **11**, 652–661 (2001).

[48] Strutt, D. Frizzled signalling and cell polarisation in Drosophila and vertebrates. *Development* **130**, 4501–4513 (2003).

[49] Li, T. *et al.* Calcium signals are necessary to establish auxin transporter polarity in a plant stem cell niche. *Nature Communications* **10**, 726 (2019).

[50] Brodskiy, P. A. *et al.* Decoding Calcium Signaling Dynamics during Drosophila Wing Disc Development. *Biophysical Journal* **116**, 725–740 (2019).

[51] Fukui, H. *et al.* Bioelectric signaling and the control of cardiac cell identity in response to mechanical forces. *Science* (2021).

[52] Bilder, D. & Scott, M. P. Hedgehog and Wingless Induce Metameric Pattern in the Drosophila Visceral Mesoderm. *Developmental Biology* **201**, 43–56 (1998).

[53] Bataillé, L., Frendo, J.-L. & Vincent, A. Hox control of Drosophila larval anatomy; The Alary and Thoracic Alary-Related Muscles. *Mechanisms of Development* **138**, 170–176 (2015).

[54] Izquierdo, E., Quinkler, T. & De Renzis, S. Guided morphogenesis through optogenetic activation of Rho signalling during early Drosophila embryogenesis. *Nature Communications* **9**, 2366 (2018).

[55] Crickmore, M. A., Ranade, V. & Mann, R. S. Regulation of Ubx Expression by Epigenetic Enhancer Silencing in Response to Ubx Levels and Genetic Variation. *PLOS Genetics* **5**, e1000633 (2009).

[56] Preibisch, S. *et al.* Efficient Bayesian-based multiview deconvolution. *Nature Methods* **11**, 645–648 (2014).

[57] Phelps, C. B. & Brand, A. H. Ectopic Gene Expression inDrosophilaUsing GAL4 System. *Methods* **14**, 367–379 (1998).

[58] Team, T. G. D. GIMP (2019).

[59] Crane, K., de Goes, F., Desbrun, M. & Schröder, P. Digital geometry processing with discrete exterior calculus. In *ACM SIGGRAPH 2013 courses*, SIGGRAPH '13 (ACM, New York, NY, USA, 2013).

[60] Thielicke, W. & Sonntag, R. Particle Image Velocimetry for MATLAB: Accuracy and enhanced algorithms in PIVlab. *Journal of Open Research Software* **9**, 12 (2021).

[61] Thielicke, W. & Stamhuis, E. PIVlab – Towards User-friendly, Affordable and Accurate Digital Particle Image Velocimetry in MATLAB. *Journal of Open Research Software* **2**, e30 (2014).

[62] Marsden, J. E. & Hughes, T. J. R. *Mathematical Foundations of Elasticity* (Dover Publications, New York, 1994), revised edn.

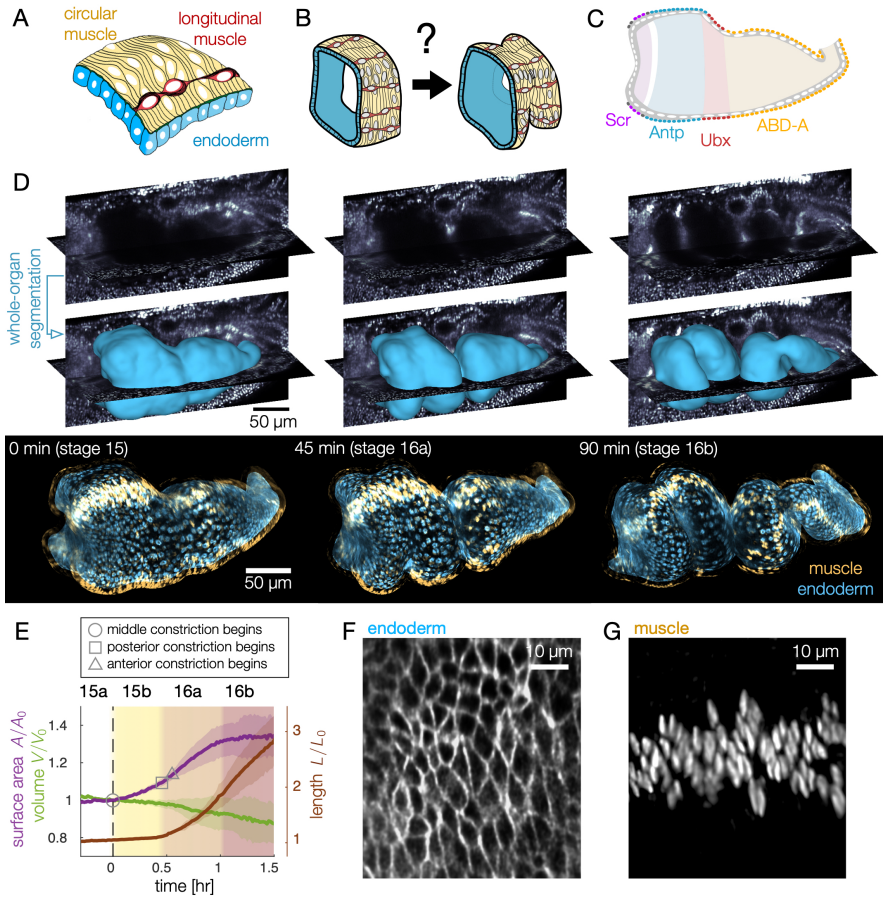

Figure 1: **Deep tissue live imaging reveals bilayer gut morphogenesis.** *(A-B)* Muscle and endoderm layers compose the midgut and interact to generate 3D shape. *(C)* Genetic patterning of hox transcription factors that govern midgut morphogenesis appears in the circumferential muscles. *(D)* Automatic segmentation using morphological snakes level sets enables layer-specific imaging, here shown for muscle (yellow) and endoderm (blue) for a *w,Hand>GAL4;UAS-Hand:GFP;hist:GFP* embryo. Morphogenesis proceeds first with a constriction cleaving the gut into two chambers (stage 15b). Two more constrictions form a total of four chambers (16a) before the gut begins to coil (16b onward). Stages follow [26]. *(E)* Surface area of the apical surface increases gradually during constrictions, but levels off by stage 16b. The enclosed volume decreases gradually, while the effective length of the organ – computed via the length of a centerline – nearly triples. Solid curves denote mean and shaded bands denote standard deviation ($N = 6$). *(F-G)* Segmentation of the endoderm layer from MuVi SPIM imaging resolves individual cells, both in the endoderm and muscle layers, shown here at stage 15a.

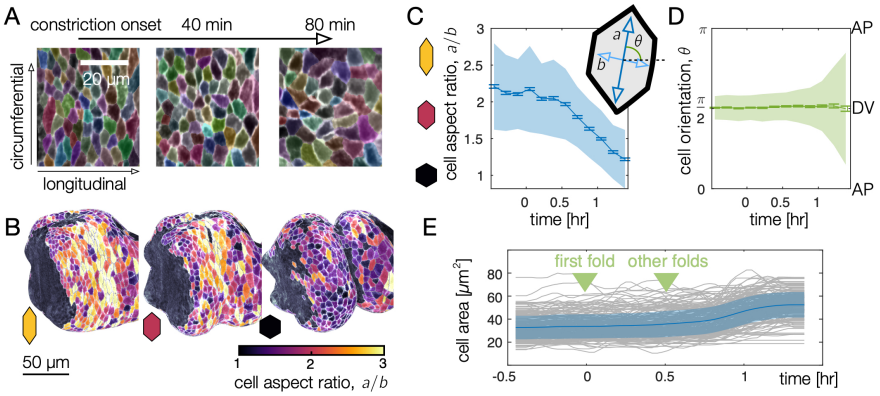

Figure 2: **Endodermal cell shape changes underlie organ shape change.** *(A)* Cell segmentation in a computationally flattened coordinate patch shows endodermal cells are initially elongated along the circumferential direction but change their shape during organ folding. *(B-C)* Cell aspect ratios evolve from $a/b > 2$ to $a/b \approx 1$, shown in 3D for cells near the anterior fold. *(C)* Colored bands denote area-weighted standard deviations for 600-1300 segmented cells per timepoint, and tick marks denote standard error on the mean. *(D)* As cells change their aspect ratio, their orientations do not rotate. *(E)* Single-cell tracking shows gentle increase of cell areas through violent folding events, suggesting that cell area changes do not drive organ shape change. Blue curve and shaded region denote mean and standard deviation, with raw traces in gray.

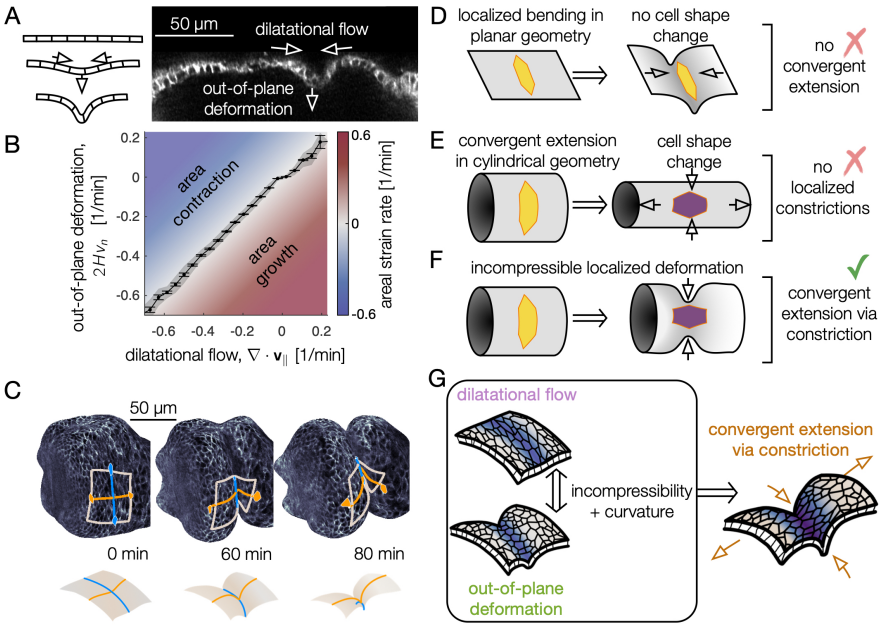

Figure 3: **Incompressible tissue dynamics reveal convergent extension via constrictions.** *(A)* Localized constrictions couple dilatational in-plane velocity patterns to out-of-plane deformation near folds. *(B)* In-plane divergence and out-of-plane deformation are correlated at the 97% level, signaling nearly incompressible behavior ($N = 3$ embryos, with kinematics sampled in 320 non-overlapping tissue patches per minute for $0 < t < 90$ min). Gray band denotes standard deviation and ticks denote standard error on the mean for each bin. Here, H denotes mean curvature, v_n is the normal (out-of-plane) velocity, and $\nabla \cdot \mathbf{v}_{\|}$ is the covariant divergence of the in-plane velocity. *(C)* The tissue converges along the circumferential direction as cells sink into the constriction (blue) and extends along the bending longitudinal profile (orange) to preserve the area of a tissue patch. *(D)* In contrast to the curved gut, localized bending of a flat, incompressible sheet requires no cell shape change, and thus no tissue-scale convergent extension. *(E)* Cell shape deformations converging along the circumferential axis and extending along the the AP axis would generate tissue convergent extension corresponding to uniform constriction of a tube, but no localized constrictions would form. *(F)* Localized constriction of an incompressible sheet exhibits cell shape change without cell area change in the absence of oriented divisions or oriented cell intercalations. The cell shape extends along the bending longitudinal (AP) axis. *(G)* Convergent extension via constriction follows as a geometric consequence of localized constrictions of the tubular organ without local area change.

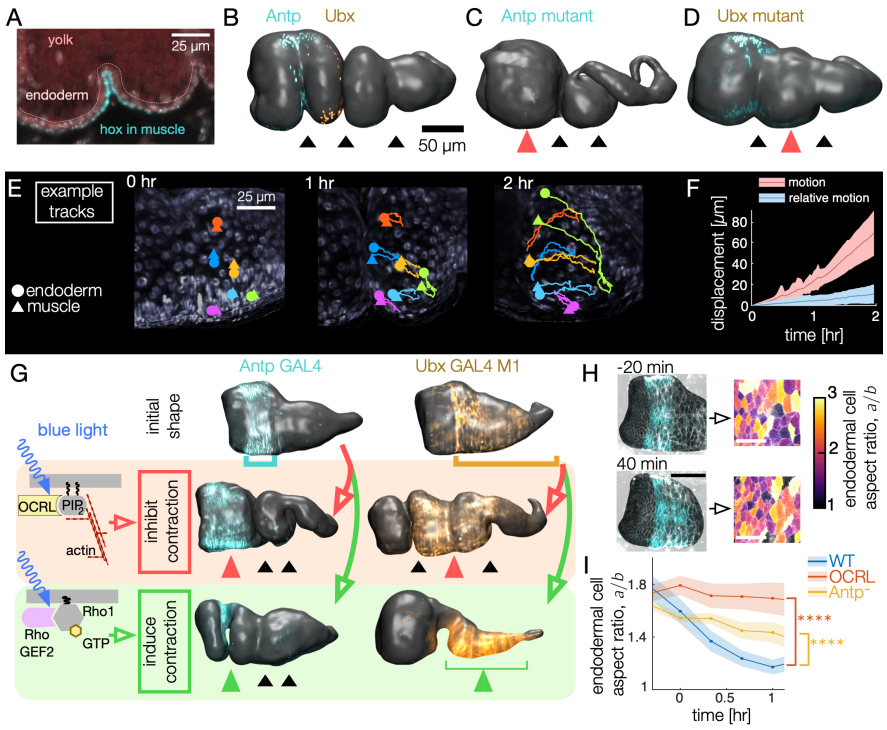

Figure 4: **Muscle contractions mechanically couple to the endoderm layer, inducing cell shape change and convergent extension.** *(A-B)* Hox genes *Antp* and *Ubx* are expressed in the circumferential muscle in discrete regions, shown for surfaces extracted from light-sheet imaging. *(C-D)* Hox genes control organ shape: *Antp* and *Ubx* mutants lack anterior and middle constrictions, respectively. *(E)* Muscle and endoderm layers move together. By computationally extracting both muscle and endoderm layers in an embryo expressing both fluorescent circumferential muscle and endoderm (*w,Hand>GAL4;UAS-Hand:GFP;hist:GFP*), we track relative motion of initially close muscle-endoderm nuclei pairs. *(F)* Muscle-endoderm nuclei pairs show modest relative motion compared to the integrated motion of the tissue ($N = 81$ pairs, colored bands denote standard deviations). *(G)* Optogenetic inhibition of contractility via *CRY2-OCRL*, which dephosphorylates PI(4,5)P_2 [18], mimics hox mutant behaviors ($N = 11$ each), and stimulation of muscle contraction via recruitment of *CRY2-ρGEF2* to the plasma membrane [54] drives ectopic folding ($N = 5$ each). *(H)* Inhibiting muscle contraction via *CRY2-OCRL* prevents endoderm cell shape change, shown for snapshots before and after the anterior constriction would normally form. The black scale bar is 50 μm, and white scale bar in images of segmented cells is 25 μm. *(I)* Measurements of endodermal cell anisotropy over time confirm that mechanical inhibition in the muscle reduces cell shape change in the endoderm (blue, $p = 1 \times 10^{-22}$). *Antp* mutants also exhibit reduced endoderm cell shape change, consistent with *Antp* regulating muscle contraction (yellow, $p = 4 \times 10^{-9}$). Each datapoint is the weighted average of multiple adjacent timepoints from 2-3 embryos with at least 30 cells per timepoint segmented in each embryo. Colored bands denote standard error on the mean.

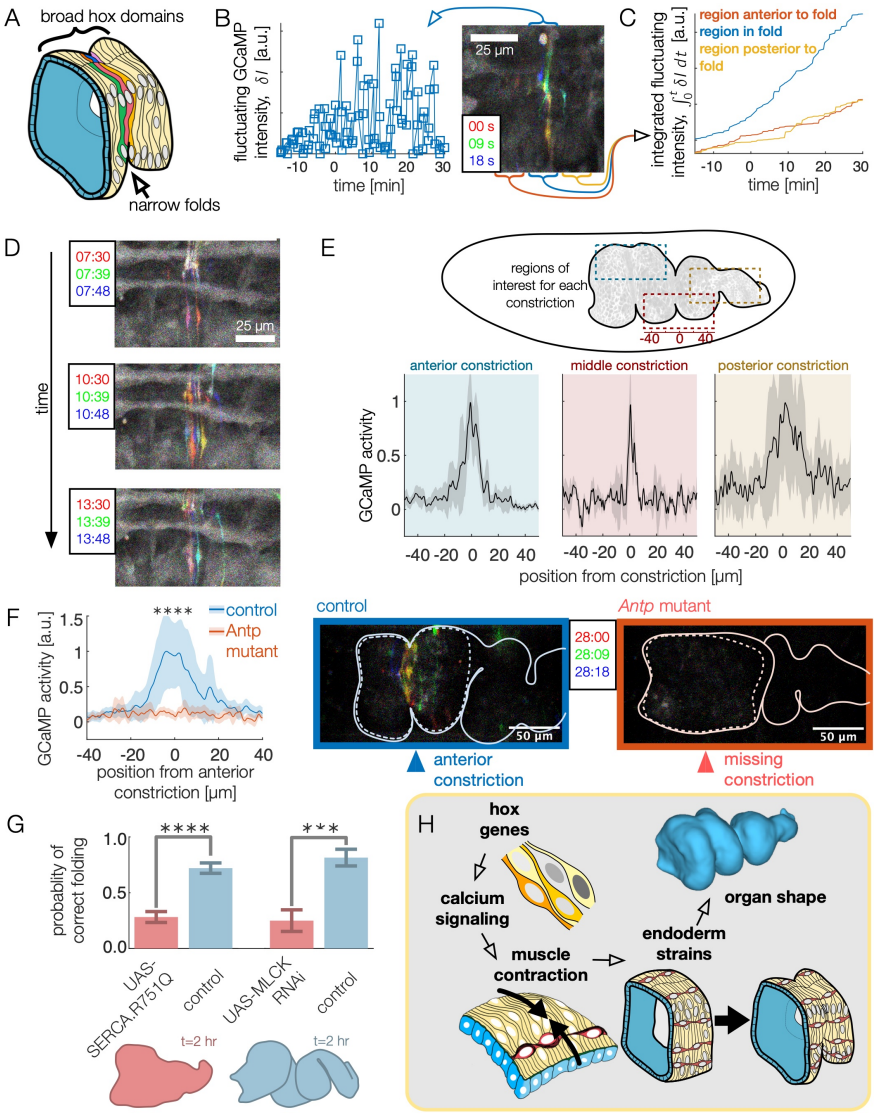
A
broad hox domains
narrow folds
B
fluctuating GCaMP intensity, δI [a.u.]
time [min]
25 µm
00 s
09 s
18 s
C
integrated fluctuating intensity, ∫δI dt [a.u.]
region anterior to fold
region in fold
region posterior to fold
time [min]
D
time
07:30
07:39
07:48
10:30
10:39
10:48
13:30
13:39
13:48
25 µm
E
regions of interest for each constriction
anterior constriction
middle constriction
posterior constriction
GCaMP activity
position from constriction [µm]
F
GCaMP activity [a.u.]
control
Antp mutant
****
position from anterior constriction [µm]
control
Antp mutant
28:00
28:09
28:18
50 µm
anterior constriction
missing constriction
G
probability of correct folding
****
***
UAS-SERCA.R751Q
control
UAS-MLCK RNAi
control
t=2 hr
t=2 hr
H
hox genes
calcium signaling
organ shape
endoderm strains
muscle contraction

Figure 5: **High frequency calcium pulses mediate muscle contraction, linking hox genes to organ shape through tissue mechanics.** *(A)* Dynamic calcium pulses appear near the anterior fold, localized to a region more narrow than the *Antp* domain. *(B)* Transient pulses in *GCaMP6s* intensity occur on the timescale of seconds and increase in amplitude when folding begins ($t = 0$). Red, green, and blue channels of images represent maximum intensity projections of confocal stacks separated in time by 9 seconds, here and below. *(C)* Integrated transient pulses for the embryo in (B) show calcium pulses are localized near the fold: *GCaMP6s* signals 20μm in front (red) or behind the fold (yellow) are less intense. *(D)* Snapshots of *GCaMP6s* fluorescence in muscle cells demonstrate calcium activity near constrictions. Each frame is a composite of three subsequent snapshots in red, green, and blue, so that transient pulses appear as colored signal, while background appears gray. Different muscle cells report calcium activity in adjacent frames. *(E)* Average fluorescent activity during the first 15 minutes of folding show localized signatures at each constriction, with particularly sharp peaks in the middle and anterior constrictions ($N = 5$, $N = 2$, and $N = 7$ for anterior, middle, and posterior folds, respectively). *(F)* In *Antp* mutants, *GCaMP6s* fluorescence is significantly reduced ($p = 2 \times 10^{-8}$) and is not localized in space. Snapshots of *GCaMP6s* expression 28 minutes after posterior fold onset (right) show almost no activity in the anterior region compared to the control (left). *(G)* Disruption of calcium regulation in muscle cells inhibits constrictions. The probability of forming three folds is reduced under heat-shock induced expression of the dominant negative mutant allele *SERCA.R751Q* with a muscle-specific driver *Mef2-GAL4* ($N = 130$, $p = 7 \times 10^{-9}$), and is likewise reduced under RNA interference of MLCK driven by *tub67-GAL4; tub16-GAL4* ($N = 37$, $p = 2 \times 10^{-4}$). *(H)* Altogether, we infer that hox genes are upstream of patterned calcium pulses, which generate muscle contraction that is mechanically coupled to the endoderm, driving tissue strains and ultimately organ shape.

Materials and Methods

Stocks and reagents

For this work, we used the following stocks based on Bloomington Drosophila Stock Center stocks: *w; 48Y-GAL4; klar*, *w; UAS-CAAX::mCherry; +*, *w; UAS-histone::RFP*, *UAS-MLCK RNAi TRiP VALIUM 20*, *y,w,Antp-GAL4; +; klar*, *w; sqh GFP; +*. *w[*]; I-76-D, Ubx*$^{9.22}$ *e*^{1}*/TM6B, Tb Df(3R)Antp*$^{NS+RC3}$. Additional stocks used were *w; +; Mef2-GAL4* (a gift from Lucy O'Brien), *w[*]; UASp-CIBN::pmGFP; UASp-mCherry::CRY2-OCRL* (a gift from Stefano de Renzis), *w[*]; UASp-CIBN::pmGFP; UASp-RhoGEF2-CRY2::mCherry* (a gift from Stefano de Renzis), *Hand-GFP; 4xUAS-Hand; +* (a gift from Zhe Han), *w; +; Ubx-GAL4 M1* (a gift from Ellie Heckscher) [43, 55], *w; +; Ubx-GAL4 M3* (a gift from Ellie Heckscher) [43, 55], *w; tub67-GAL4;tub15-GAL4* (a gift from Eric Wieschaus), and *w; +; Gap*^{43} *mCherry* (a gift from Eric Wieschaus).

We used following antibodies for staining: Ubx FP3.38 (diluted 1:10, Developmental Studies Hybridoma Bank), Antp 8C11 (diluted 1:25, Developmental Studies Hybridoma Bank), anti-ABDA C11 (dilued 1:50, Santa Cruz Biotechnology).

Microscopy

For light sheet imaging of live and fixed embryos, we used a custom multi-view selective plane illumination microscope drawn schematically in Fig. 1 - supplement 1A. This setup has been previously described in [7].

Subsequent registration, deconvolution, and fusion using the methods presented in [56] results in a single, deconvolved data volume per timepoint with isotropic resolution (0.018 μm^3 per voxel). For most experiments in this work, we acquire one volume per minute. The optimal number of deconvolution iterations varied between 8 and 20 for different fluorescent reporters. We used 6 or 8 views for most datasets.

To peer deep inside the developing embryo, we leverage the UAS-GAL4 system [57] to express fluorescent proteins in gut-specific tissues and use embryos with the *klarsicht* mutation [28], which reduces scatter without altering gut morphogenesis. Video 1 shows a maximum intensity projection of the left lateral half data volume for a deconvolved nuclear marker in the midgut as a complement to Figure 1 of the main text. In Video 1, non-midgut tissues expressing *48Y GAL4* are largely masked out using an iLastik training to darken voxels far from the gut, but some cells outside the midgut that express *48Y GAL4* are visible on the dorsal side.

We used confocal microscopy (Leica SP8) for more detailed characterization of calcium dynamics, live imaging of *Ubx* and *Antp* mutants, and supplementary optogenetic experiments.

Parameterization of the organ shape

To quantify geometry of organ shape and deformation, we built an analysis package called TubULAR [32]. While details of the publicly-available, open source package are included in [32] and the associated repository (), here we describe our use of the package for the presented results.

We begin by using TubULAR's surface detection methods to extract the organ shape with a morphological snakes level set analysis [30, 31] on the output of an iLastik training [29] against midgut tissue (membrane, nuclei, actin, or myosin). Example results from this segmentation performed on a *w;48Y GAL4/UAS-CAAX::mCh* embryo are shown in midsagittal sections in Fig. 1 - supplement 2. We then use TubULAR's cartographic mapping functions to map the surface to the plane and stabilize noise in the mappings' dynamics [32]. For visualization, we use a pullback parameterization (s, ϕ) such that the coordinate directions $(\hat{s}, \hat{\phi})$ are determined by the conformal mapping to the plane at the onset of the first constriction ($t = 0$). In this way, ϕ parameterizes the intrinsic circumferential axis and s parameterizes a longitudinal position along the long axis of the organ at $t = 0$. In subsequent timepoints, the difference in param-

eterization coordinates in 3D space are minimized to match the previous timepoint, such that the coordinates follow the shape change of the organ [32]. We find this (s, ϕ, t) parameterization aids in both visualization and enables more accurate velocimetry measurements than other choices.

We define the 'material frame' of a given midgut as the tissue configuration at the onset of the middle constriction, which is the first constriction that appears.

We compute the centerline using the TubULAR package [32], wherein the organ is divided into circumferential 'hoops' based on its planar parameterization (Fig. 1 - supplement 3). Hoops for which s =constant define an effective circumference for increments along the length of the organ, and the average 3D position of each hoop defines its centerline point. Connecting mean points of adjacent hoops along the length of the organ defines the centerline of the object (brown curve) whose length is reported in the main text Figure 1E.

Endodermal cell segmentation and shape change

Using a single slice of the gut surface projected into stabilized (s, ϕ) pullback coordinates, we segmented 600-1300 cells per timepoint (Fig. 2 - supplement 1) using a semi-automated procedure:

1. We first perform adaptive histogram equalization over patches of the pullback containing several cells in width.

2. We then perform two passes of morphological image reconstruction (see MATLAB's `imreconstruct` function) punctuated by morphological dilation and erosion steps.

3. The result is binarized and skeletonized via a watershed algorithm.

4. We overlay this skeleton on the original image to enhance the membrane contrast, convolve with a narrow Gaussian (with a standard deviation of $\sim 0.2\%$ of organ length), and

pass the result through the previous three steps.

This gives us an estimate for the image segmentation. We then manually correct any spurious segmentation artifacts in GIMP [58] by overlaying the segmentation with the original pullback images. To resolve some ambiguous cell junctions, we examine not only a single slice of the endodermal cell layer near the apical side (about 2.5μm beyond the apical side), but also the maximum intensity projection of several microns along the surface normal direction.

We compute cell anisotropy by finding segmented cell shapes in 2D, embedding those polygons in 3D, projecting each cell onto a local tangent plane, and measuring the moment of inertia tensor of this polygon in the material coordinate system. This procedure is shown schematically in Fig. 2 - supplement 1. We then embed the Lagrangian coordinate directions $(\hat{s}, \hat{\phi})$ from a conformal mapping of the whole organ at the onset of the initial (middle) constriction $t = t_0$ onto the cell's centroid in 3D (in the deformed configuration at time $t \neq t_0$). The moment of inertia tensor for the cell polygon is expressed in the local coordinate system from the embedded $(\hat{s}, \hat{\phi})$ directions in the local tangent plane of the tissue. The eigenvalues I_1 and I_2 of the moment of inertia tensor and their associated eigenvectors then provide an effective ellipse for the cell with orientation θ with respect to the local $\hat{\mathbf{s}}$ direction and an aspect ratio $a/b \equiv \sqrt{I_1/I_2}$. Fig. 2 - supplement 1 shows the raw data of these measurements without computing statistics.

We then average the cellular anisotropy over the organ surface to report a mean, standard deviation, and standard error for both the cellular aspect ratio and cell orientation. In this averaging, we weight each cell's contribution to the observable (aspect ratio a/b or orientation θ) by its area, so that all material points on the organ are given equal weight. The results reported in Figure 2C and D in the main text are the weighted mean and weighted standard deviation for

each distribution. The weighted means of the aspect ratio a/b and orientation θ are

$$\langle a/b \rangle = \frac{\sum_{i=1}^{N} A_i a_i/b_i}{\sum_{i=1}^{N} A_i} \tag{2}$$

$$\langle \theta \rangle = \tan^{-1}\left[\frac{\sum_{i=1}^{N} A_i \sin\theta_i}{\sum_{i=1}^{N} A_i \cos\theta_i}\right], \tag{3}$$

where A_i is the area of the i^{th} cell, and N is the total number of cells. We note that we obtain similar results by weighting each cell equally, which would correspond to setting $A_i = 1$ for all i above.

We obtain standard errors by bootstrapping. In detail, we subsample our collection of measurements, compute the weighted mean for the subsample, and repeat with replacement 1000 times. The variance of these 1000 means decreases in proportion to the number of samples n included in our subsampling, so that $\sigma_{\overline{x}}^2(n) = \tilde{\sigma}_{\overline{x}}^2/n + \sigma_0^2$. Fitting for $\sigma_{\overline{x}}^2$ across 50 values of n ($N/4 < n < N$) and evaluating this fit for $n = N$ gives an estimate for the standard error on the mean $\sigma_{\overline{x}} = \sqrt{\sigma_{\overline{x}}^2}$. In practice, the result is nearly identical to measuring the means of many weighted subsamplings of $n = N$ cells with replacement and computing the standard deviation of this collection of means.

Single-cell tracking

We tracked 175 cells from -27 min $< t < 83$ minutes of development relative to the onset of the middle constriction in a *w; 48Y GAL4;klar* $\times$ *w; UAS-CAAX::mCh* embryo imaged using confocal MuSPIM. First, we segmented the same 175 cells in the first chamber of the gut every two minutes using the same procedure as in the previous section. We tracked their positions over time using iLastik manual tracking workflow using 2D (s, ϕ) pullback projections. From these segmented polygons, we project back into 3D onto the gut surface and measure the cell areas in a local tangent plane for Figure 2E in the main text.

Topological cell rearrangements in the endoderm

Cell rearrangements are also present in the endodermal tissue, and these 'T1' events could also contribute to the large-scale shear [34]. To estimate their contribution, we performed manual tracking of 175 segmented cells in the first chamber and identified T1 transitions from $-27 < t < 83$ minutes relative to the onset of the middle constriction. Importantly, the orientation of T1 transitions is not significantly aligned with the elongation axis at early times, suggesting that the endoderm is fluidized and that T1s are not a tightly controlled process directing morphogenesis.

To identify T1 transitions, we leveraged our single-cell tracking previously used in Fig. 2E – a contiguous region of cells in the anterior chamber of the midgut, extending from the anteriormost portion of the midgut up to the anterior fold. We query all cell pairs which share an edge in the endoderm at any time during the morphogenetic process. We then filter out any pairs that remain neighbors for all timepoints, since their shared edges do not participate in topological rearrangements. The remaining pairs reflect a cell-cell interface which either appears or vanishes during morphogenesis. We perform additionally screening of these candidate events to confirm that the change in cell topological is not an artifact from possible segmentation error by coloring the two cells participating and visually inspecting their motion. Video 5 and Fig. 2 - supplement 3 show an example sequence of T1 transitions tracked using this scheme.

For each junction lost or gained, we measure the axis of the associated T1 transition by computing the centroid of each cell in the pair that is gaining or losing a junction. Fig. 2 - supplement 3B shows a histogram of these axes' angles with respect to the anterior-posterior axis of the organ defined in a locally conformal coordinate patch, with the AP axis orientation inferred from the material (Lagrangian) frame. We find that T1 transitions oriented along the AP axis (converging along DV) occur about as frequently as T1 transitions oriented along the DV axis (converging along AP) for our collection of tracked cells in the first lobe, suggesting that topological cell rearrangements are not a principal driver of convergent extension in the

tissue. These rearrangements are therefore unlikely to drive shape change, as predicted by the quantitative similarity between tissue shear and cell shape change (Fig. 3 - supplement 5).

Quantification of tissue deformation

To compute a coarse-grained tissue velocity over the gut surface, we again used the TubULAR package [32]. This resource enables velocimetry and discrete exterior calculus measurements [59] on the evolving surface. The result is a fully covariant measurement of the compressibility and shear of the tissue spanning the whole organ.

Briefly, given our (s, ϕ, t) coordinate system defined in the TubULAR pipeline, we then run particle image velocimetry (PIV) using PIVLab [60, 61] and map tissue velocities in the domain of parameterization to the embedding space. Geometrically, displacement vectors $\mathbf{v}$ extend from one $\mathbf{x}(s_0, \phi_0, t_0)$ coordinate in 3D on the surface at time t_0 to a different $\mathbf{x}(s_1, \phi_1, t_1)$ coordinate on the deformed surface at time t_1. When t_0 and t_1 are adjacent timepoints, this defines the 3D tissue velocity at $\mathbf{x}(s_0, \phi_0, t_0)$ as $\mathbf{v}(s_0, \phi_0, t_0) = (\mathbf{x}(s_1, \phi_1, t_1) - \mathbf{x}(s_0, \phi_0, t_0))/(t_1 - t_0)$. We decompose the velocity into a component tangential to the surface $\mathbf{v}_{\|}$ and a normal component $\mathbf{v}_n = v_n \hat{\mathbf{n}}$ for measuring divergence via discrete exterior calculus [32] and for measuring out-of-plane deformation $2Hv_n$, where H is the mean curvature obtained via computing the Laplacian of the mesh vertices in (embedding) space: $\Delta \mathbf{X} = 2H\hat{\mathbf{n}}$ (see [59]).

As shown in Fig. 3 - supplement 1, the in-plane dilatational flow almost perfectly matches the out-of-plane deformation during the morphogenetic process. We make sense of dilatational flow and out-of-plane deformation and interpret their difference as the local area growth rate by the following argument. The surface changes according to its tissue velocity, which has tangential and normal components $\mathbf{v} = \partial_t \mathbf{X} = v^i \mathbf{e}_i + v_n \hat{\mathbf{n}}$. The shape of the surface is encoded by the metric $g_{ij} = \partial_i \mathbf{X} \cdot \partial_j \mathbf{X}$, which describes lengths and angles measured in the tissue, and by the second fundamental form $b_{ij} = \partial_i \partial_j \mathbf{X} \cdot \hat{\mathbf{n}} = -\partial_i \mathbf{X} \cdot \partial_j \hat{\mathbf{n}}$, which contains information relating

to both intrinsic and extrinsic measures of surface curvature [59]. The time rate of change of the metric is determined by the superposition of velocity gradients and normal motion where the surface is curved [35, 62]:

$$\partial_t g_{ij} = \nabla_i v_j + \nabla_j v_i - 2 v_n b_{ij}. \tag{4}$$

Here, ∇ denotes the covariant derivative operator defined with respect to the embedding metric $\mathbf{g}$. The covariant mass continuity equation gives [35]

$$0 = \frac{D\rho}{Dt} + \frac{\rho}{2}\mathrm{Tr}[\mathbf{g}^{-1}\dot{\mathbf{g}}] \tag{5}$$

$$= \frac{D\rho}{Dt} + \rho \nabla \cdot \mathbf{v}_{\|} - \rho 2 v_n H, \tag{6}$$

where ρ is the mass density in the physical embedding, and the material derivative is $D\rho/Dt = \partial_t \rho + \rho(\nabla \cdot \mathbf{v}_{\|}) + \mathbf{v} \cdot \nabla \rho$. Incompressibility ($D\rho/Dt = 0$) then implies

$$2 H v_n = \nabla \cdot \mathbf{v}_{\|}. \tag{7}$$

Minimal ingredients demonstrate geometric interplay between compressibility and shear

A flat, nearly incompressible sheet demonstrates a kinematic coupling between dilatational in-plane flow ($\nabla \cdot \mathbf{v}_{\|}$) and out-of-plane deformation ($2Hv_n$). Contracting such a sheet as in Fig. 3 - supplement 3A leads to out-of-plane bending to preserve surface area of the sheet. This out-of-plane motion leaves cells unchanged in their aspect ratio: no in-plane deformation is necessary.

If the sheet is curved into a tube (so that mean curvature is nonzero, $|H| > 0$), then constricting an sheet (with inward velocity $v_n > 0$) can generate deformation in the local tangent plane of the sheet. Such incompressibility couples to initial curvature to generate shear deformation. For example, an incompressible sheet of paper glued into a cylinder along one of its edges cannot be pinched in this fashion without crumpling, folding, or tearing. An elastic sheet,

however, can be deformed in this manner even if local areas of material patches are required not to change. In particular, the sheet may stretch along the long axis while constricted circumferentially, such that a circular material patch is transformed into an elliptical patch with the same area, as in Fig. 3 - supplement 3B.

Finally, these two effects are coupled in the case of the pinched cylinder. In a given snapshot with an existing localized constriction, we can schematically understand the three ingredients by considering the pinched cylinder with a step-wise indentation shown in Fig. 3 - supplement 3C. First, active stresses constrict the neck, decreasing the surface area of the neck (blue) and dilating the interior faces (red). In order to restore the surface area of the cells in the neck, its length may increase, resulting in extension along the long axis of the tube. In tandem, to combat the dilation in the interior faces, cells flow into the constriction from the chambers. Note that if all three steps are instantaneously coupled, the order of events is immaterial to the outcome: contractile surface flows could increase the density of cells in the interior faces, which leads to neck constriction to restore cell density in the faces and results in convergent extension of the neck.

We note also that when the constriction is broad along the longitude or when the indentation is shallow, the mean curvature will be positive everywhere (cylinder-like, $H > 0$). In this case, inward motion of the incompressible tube causes an extensile surface flow ($\nabla \cdot \mathbf{v}_{\|} > 0$), rather than a contractile one. This is a qualitative difference between broad or uniform constrictions of a tube and localized constrictions such as those seen in the midgut. In principle, we predict a crossover between the two modes of behavior during the very onset of constriction in our system – from positive to negative divergence as the curvature changes sign. This is a subtle and transient feature, given the large radius of the midgut compared to the small axial length of the constrictions and the non-uniform initial curvature of the midgut before constrictions begin.

Quantification of tissue shear

We employ a geometric method of tissue-scale shear quantification that accounts for both the shear due to the changing shape of the gut and the shear due to the material flow of cells along the dynamic surface. The first step is to establish consistent material coordinates for all times, i.e. labels for parcels of tissue that follow those parcels as they move and deform. We prescribe these labels at the onset of midgut constrictions by endowing a cylindrical 'cut mesh' of the organ's surface at the that time with a planar parameterization. The cut mesh is first conformally mapped into a planar annular domain, $\{||\mathbf{x}|| : r \leq ||\mathbf{x}|| \leq 1\}$, using a custom Ricci flow code included in our TubULAR package [32]. Fixing the outer radius of the annulus to 1, the inner radius r is a conformal invariant that is automatically determined from the geometry of the organ. Taking the logarithm of these intermediate coordinates then defines a rectangular domain, with a branch cut identifying the top and bottom horizontal edges of the domain in such a way the the cylindrical topology of the cut mesh in 3D is fully respected. The coordinates in this domain are taken to be the material ('Lagrangian') coordinate system, $(\tilde{\zeta}, \tilde{\phi})$. This conformal parameterization is, by construction, isotropic; the metric tensor is diagonal. This parameterization is therefore a suitable reference against which to measure all subsequent accumulation of anisotropy in the tissue. We note that at the reference time t_0 (at the onset of the first constriction), the material coordinates are similar to the (s, ϕ, t_0) coordinate system defined before, except that the coordinate s measures a proper length on the surface along curves of constant ϕ, while $\tilde{\zeta}$ is a coordinate of the conformally mapped planar domain. We chose to use s instead of $\tilde{\zeta}$ for visualizations simply because deep constrictions exhibit extreme dilation in a conformal $(\tilde{\zeta}, \tilde{\phi})$ pullback plane, but these are attenuated in an (s, ϕ) pullback plane (see [32]). We stress that all measurements account for the physical embedding of the surface: the coordinate system parameterizing the surface is a tool to define circumferential and longitudinal directions based on the organ's intrinsic geometry, and the choice of parameterization does not influence the

magnitude of tissue deformation.

In order to recapitulate the material flow of the tissue, these coordinates are advected in the plane along the flow fields extracted using PIV [61, 60] and then mapped into 3D at each time point. This mapping defines a deformed mesh whose induced metric tensor, $\mathbf{g}' \equiv \mathbf{g}(t)$, can be computed relative to the material coordinates. All anisotropy in the mapping is encoded by the complex Beltrami coefficient, $\mu(t)$, defined in terms of the components of the time-dependent metric tensor

$$\mu(t) = \frac{g'_{11} - g'_{22} + 2i\, g'_{12}}{g'_{11} + g'_{22} + 2\sqrt{g'_{11}\, g'_{22} - {g'_{12}}^2}}. \tag{8}$$

As illustrated in Fig. 3 - supplement 4B, μ describes how an initially circular infinitesimal patch of tissue is deformed into an elliptical patch under the action of the material mapping. The argument of μ describes the orientation of this ellipse. The magnitude $|\mu|$ is related to the ratio, K of the lengths of the major axis of this ellipse to its minor axis by

$$K = \frac{1 + |\mu|}{1 - |\mu|}. \tag{9}$$

When $|\mu| = 0$, the material mapping is isotropic, i.e. a circular patch of tissue remains circular under the mapping. Note that $|\mu| < 1$ and therefore provides a bounded description of both the magnitude and orientation of material anisotropy in the deforming surface.

The results of this measurement are shown as a kymograph in Fig. 3 - supplement 4 for a representative dataset. Constrictions begin to appear at times and locations marked by red arrows and continue to deepen. The Beltrami coefficient is averaged along the circumferential direction and plotted at the anterior-posterior position in tissue coordinates at the onset of the middle constriction (the first constriction to appear), so that the deformation of advected tissue patches are compared to their original shape. A single color dominates the kymograph, indicating that the deformation is globally aligned to extend along the local longitudinal axis (and contract along the material frame's circumferential axis), despite the contorting and com-

plex shape. This is consistent with circumferential muscle orientations defining the axes for convergent extension in the midgut.

Relative motion between layers

To characterize relative motion between layers, we tracked 375 endodermal and 81 muscle nuclei in the same *w,Hand>GAL4;UAS-Hand:GFP;hist:GFP* embryo. Fig. 4 - supplement 1 shows measurements of relative displacement of initially-close nuclei pairs (< 5 μm apart at the onset of the first constriction). Two example tracks are highlighted in yellow and green. Fig. 4 - supplement 2 shows additional statistics of the relative motion over time.

Optogenetic experiments

The *UAS-CRY2-OCRL* and *UAS-ρGEF2* constructs have been previously characterized [18, 54]. For optogenetic confocal microscopy experiments, we activated the optogenetic construct with continuous oblique illumination of a 470 nm LED at 6.2$\pm$0.1 mW/cm^2 power, in addition to periodic illumination with the 488 nm laser used to image the sample. Wild-type embryos developed normally under this illumination ($N = 18/19$). Variations by a factor of two in either the LED power or in the 488 nm laser power used to image the *GFP* channel did not result in differences in phenotype. For light sheet imaging, we illuminated with a 488 nm laser line at 1 mW for 30 seconds once per minute.

We quantified the endoderm cell shapes using a similar procedure as before. After deconvolution (Huygens Essential software), we perform 3D segmentation via a morphological snakes level set method on an iLastik pixel classification to carve out an approximate midsurface of the endoderm. We measured the endoderm shape dynamics for two-color *y,w,Antp-GAL4;;Gap*^{43} *mCherry* $\times$ *w;UAS-CIBN::GFP;UAS-CRY2-OCRL* embryos held under continuous optogenetic activation from oblique illumination of a 470 nm LED at 6.2$\pm$0.1 mW/cm^2 power as before. For

comparison, we additionally measured endoderm shapes in *Antp* mutant embryos with a membrane marker driven in the midgut endoderm (*w;48Y GAL4/UAS-CAAX::mCh;Antp*$^{NS+RC3}$).

Fig. 4 - supplement 3A shows representative snapshots of this segmentation procedure for a two-color *y,w,Antp-GAL4;;Gap*^{43} *mCherry* $\times$ *w;UAS-CIBN::GFP;UAS-CRY2-OCRL* embryo at the onset of the first constriction and 40 minutes after the middle constriction began. Circumferential muscle localized near the anterior constriction expresses the optogenetic construct (cyan band), while the endoderm is imaged using a ubiquitous membrane marker (grayscale). Image regions masked in semi-transparent gray are the deepest confocal plane acquired, while the rest of the image is a lateral view of the projected data on the segmented organ surface. Segmented endodermal cell polygons are colored by their aspect ratios. Cells are segmented in 2D and then projected into 3D for measurement of their aspect ratios. As shown in Fig. 4 - supplement 3C, there is no significant difference between cell orientations in wild-type (blue), optogenetic mutants (red), and *Antp* mutants (yellow).

Wild-type calcium dynamics

We quantified calcium dynamics using the confocal microscopy (Leica SP8) of the live reporter *UAS GCaMP6s* driven by either the driver *Mef2-GAL4*, which is expressed across all muscles in the embryo, or *48Y GAL4*, which is expressed in the embryonic midgut both in endoderm and visceral muscles. Here, we used *Mef2-GAL4* as a driver for characterizing anterior and middle constrictions. We used *48Y GAL4* for the posterior constriction since many fluorescent somatic muscles occlude the line of sight for the posterior constriction under *Mef2-GAL4*. We found that the two drivers yielded similar quantitative results for the anterior constriction.

To measure transient calcium activity without bias from variations in ambient fluorescent intensity due to spatially-dependent scattering, we imaged three confocal stacks with 2.5-3 μm step size in rapid succession (9 or 10 seconds apart) and subtracted subsequent image stacks

from each other according to

$$\delta I \equiv |I_1 - I_2| + |I_2 - I_3| + |I_1 - I_3|, \tag{10}$$

where $I_i = I_i(x, y)$ is the maximum intensity projection (projected across $dz \approx 30\mu$m) of the i^{th} stack. Over such short timescales, motion of the midgut is small, but transient flashes of *GCaMP6s* are unlikely to span more than one acquisition. We then extract coherent features from δI using a Gaussian blur followed by a tophat filter, and sum the resulting signal along the circumferential direction.

While we interrogated *GCaMP6s* activity using many views of the gut, the quantification used three standardized views. For the anterior constriction, we used a dorsal view, since out-of-plane effects are smallest on the dorsal side and since the midgut is nearest to the surface on the dorsal side. For the middle constriction, we used ventrolateral views since there is a line of sight with fewer other muscles driven by *Mef2-GAL4* from this view. For the posterior constriction, we used a left lateral view for quantification.

To time-align the *GCaMP6s* experiments of the anterior and middle constrictions, we defined $t = 0$ as the first timestamp in which the constriction under observation showed localized bending along the longitudinal (AP) axis. For characterization of calcium dynamics at the posterior constriction, we defined the onset of constriction by the ventral side of the gut visceral muscle having moved dorsally by $\sim$10 μm.

Fig. 5 - supplement 1 shows kymographs of *GCaMP6s* dynamics averaged across biological repeats. In these kymographs, activity begins near the time when constrictions begin. In contrast, Fig. 5 - supplement 3 shows delayed and suppressed *GCaMP6s* activity in *Antp* mutants compared to the wild-type behavior of sibling embryos that are not homozygous mutants for *Antp*.

Calcium activity in *Antp* mutants

To compare calcium activity in *Antp* mutants against wild-type dynamics, we computed p values using a z-score measuring the difference between *Antp* heterozygotes (controls) and *Antp* homozygotes (mutants) as

$$Z = \frac{\overline{\delta I}_{\text{mutant}} - \overline{\delta I}_{\text{control}}}{\sqrt{s^2_{\text{control}}/n_{\text{control}} + s^2_{\text{mutant}}/n_{\text{mutant}}}}, \tag{11}$$

where $\overline{\delta I}$ is the sample mean, s_{control} and s_{mutant} are the sample standard deviations, and n_{control} and n_{mutant} are the sample sizes. This score gives a single-sided p value via

$$p = \frac{1}{2}\text{erfc}\left(-Z/\sqrt{2}\right), \tag{12}$$

where erfc is the complementary error function.

To quantify the difference in overall activity between mutants and heterozygotes, we first estimate the expected fluorescent intensity for a given embryo under the null hypothesis that all embryos, whether mutant or not, will have similar *GCaMP6s* activity. Since embryos vary in opacity, we normalized each heterozygous embryo according to a value dependent on its background fluorescent intensity measured in regions within the embryo but far (45-50 μm) from the site of the putative constriction. The observed maximum fluorescent activity δI correlated with this background signal with a correlation coefficient of 78% and a mean signal-to-background ratio of 5.1$\pm$0.5. We then normalized each embryo's time-averaged $\delta I = \delta I(x)$ as

$$\delta I \to \frac{\delta I - \delta I_{\text{bg}}}{\delta I_{\text{max}} - \delta I_{\text{bg}}}. \tag{13}$$

This enabled us to reduce the confounding influence of variation in optical density between embryos in the mutant analysis and compare absolute curves δI rather than only their variation along the anterior-posterior axis.

MLCK RNAi and SERCA mutant analysis

To drive expression of MLCK RNAi or a dominant negative allele of *SERCA*, we administered heat shock by abruptly raising the temperature to 37°C using a stage-top incuabator (Okolab) and observing embryos staged such that they had not yet completed gut closure. The standard errors in the probabilities of successful constrictions are given by

$$SE = \sqrt{\frac{\hat{p}\,(1-\hat{p})}{N}}, \tag{14}$$

where $\hat{p}$ is the observed frequency of forming all three constrictions and N is the number of samples of a given genotype (for ex, *Mef2-GAL4×UAS-SERCA.R751Q::mtomato*) measured in the experimental heat shock conditions. We note that the result is not sensitive to the choice of analysis. For example, we also computed the mean number of folds formed – that is, the number of deep constrictions – for each condition and compare the two distributions, as shown in Fig. 5 - supplement 2A and B. The mean number of folds formed was reduced in both *Mef2-GAL4×UAS-SERCA.R751Q* embryos and *tub67-GAL4; tub16-GAL4×UAS-MLCK RNAi* embryos ($p = 3 \times 10^{-8}$ and $p = 0.002$, respectively).

Captions for supplementary videos

Video 1

Live imaging using confocal MuSPIM shows the shape change of the midgut as it folds into a coil of compartments. Here, we display panoramic views of fluorescently-labeled nuclei in both endoderm and muscle tissue layers of the midgut in a *w;48Y GAL4;klar* $\times$ *w;UAS-histone::RFP* embryo. Maximum intensity projections of half-volumes from left lateral (upper left), right lateral (lower left), dorsal (upper right), and ventral views (lower right) exhibit the nearly isotropic resolution of our imaging setup.

Video 2

Segmentation using computer vision techniques enables layer-specific imaging of midgut morphogenesis, highlighted here for a *w;48Y GAL4;klar* $\times$ *w;UAS-CAAX::mCh* embryo. First, a morphological snakes level set identifies the apical (inner) boundary of the midgut endoderm at a timepoint before the onset of constrictions. This surface follows the evolving shape of the organ during the subsequent dynamics. Rendering the data that intersects this dynamic surface allows us to visualize cells.

Video 3

An example tissue patch shows that tissue rearrangements in the endodermal cell layer (i.e. 'T1 transitions' or 'intercalation events') occur during gut morphogenesis. Here, the blue and green cells are not initially neighbors, but rearrange to separate the red and pink cells. Subsequently, the blue and pink cells lose their connection as well, as do the green and pink cells. Each tissue patch is generated by a rigid flattening of the surface to the plane in a manner that the map is nearly conformal near the center of the image, with metric components $g_{11} \approx g_{22} \approx 1$. T1 transitions are not biased in their orientation until late stages of morphogenesis, consistent with cell shape change being the dominant contributor to tissue shear.

Video 4

Extracted in-plane and out-of-plane tissue velocities show signatures associated with stages of shape change. The tangential (in-plane) component of the velocity ($\mathbf{v}_{\|}$, top panel) is colored by its orientation in the (s, ϕ) pullback plane described in the Materials and Methods. In this 'unwrapped' pullback plane, ventral tissue occupies the center of the image, anterior is left, and posterior is right. For example, purple regions flow towards the midgut's posterior and orange regions flow towards the anterior. Opacity of the colored signal is proportional to the magnitude of the tissue velocity. The normal (out-of-plane) component of the velocity (v_n, bottom panel) is red for motion in the endoderm's apical direction (toward the inside of the gut) and blue for motion in the basal (outer) direction. The corresponding midgut surface is shown on the left for

all timepoints.

Video 5

In-plane tissue velocities are tightly linked to out-of-plane motion, indicating nearly incompressible behavior of the composite midgut tissue. For a representative embryo, we plot the out-of-plane deformation $2Hv_n$ on the left, both as a left lateral view in 3D and in the (s, ϕ) pullback plane. Here, v_n is the normal velocity and H is the mean curvature, which is positive for a cylinder but negative for sharp folds whose outer radius of curvature is smaller than their inner circumference. In the middle column, we plot the dilatational flow for this embryo, defined as the covariant divergence of the in-plane velocity, $\nabla \cdot \mathbf{v}_{\|}$. In the right column, we plot the difference between these two quantities, which measures the rate of isotropic expansion or contraction of the tissue.

Video 6

Hox gene expression in the muscle layer regulates constrictions. Here, cell membrane in the Antennapedia (*Antp*) domain are fluorescently labeled (yellow), and all nuclei are fluorescently labeled in a separate channel (blue) using a *w,Antp-GAL4;klar* $\times$ *w;UAS-CAAX::mCh;UAS-Histone:GFP* embryo. The anterior constriction forms in the center of the *Antp* domain. Some tissues outside the midgut that express plasma membrane fluorescence are spuriously projected into the selected layer surface.

Video 7

Muscle nuclei (yellow) and endoderm nuclei (blue) move together during constrictions, reflecting a tight coupling between tissue layers. Here, we false color two selected layers of a *w,Hand>GAL4;UAS-Hand:GFP;hist:GFP* embryo in yellow (muscle layer) and blue (endoderm).

Video 8

Calcium pulses appear at the location of each constriction, shown here for a *Mef2-GAL4>UAS*

GCaMP6s embryo. We visualize the dynamics of calcium pulses by overlaying three snapshots captured nine seconds apart as red, green, and blue images for each frame. Thus, colored pixels represent transient activity reported by *GCaMP6s*. A composite frame is imaged every 90 seconds, and the timestamp is shown relative to the onset of the constriction, as monitored in a separate bright-field channel (not shown).

Video 9

In *Antp* mutants, calcium pulses are strongly reduced in intensity in the vicinity of the missing anterior constriction location. In WT embryos (top panel), calcium pulses appear at the onset of constrictions near the anterior constriction and appear in an increasingly spatially extended region as development progresses. In contrast, for *Antp* mutant embryos, calcium activity is reduced and does not exhibit an initially localized pattern (bottom panel).

Video 10

Disrupting calcium signaling in the muscle layer inhibits constrictions, shown here for an embryo expressing a dominant negative allele of SERCA (red) with a control embryo under the same conditions for reference (blue).

Data Availability Statement

We have uploaded processed data for experiments spanning all figures to FigShare, available at `https://figshare.com/authors/Noah_Mitchell/12456507` in project #137793: 'Visceral organ morphogenesis via calcium-patterned constrictions'. The original volumetric data from living imaging are each up to a terabyte in size. We therefore posted processed data on FigShare, including 2D pullback image sequences of the dynamic 3D tissue surfaces, volumetric data for small datasets, and processed tables. An interested researcher would be able to access the original data on our lab server. They would need to contact Sebastian Streichan (streicha@ucsb.edu) to be added to the server's list of users and could then

download the original data directly.

In addition to the TubULAR package detailed in reference 32, further software and scripts used to analyze the data is available at: `https://github.com/npmitchell/VisceralOrganMorpho`

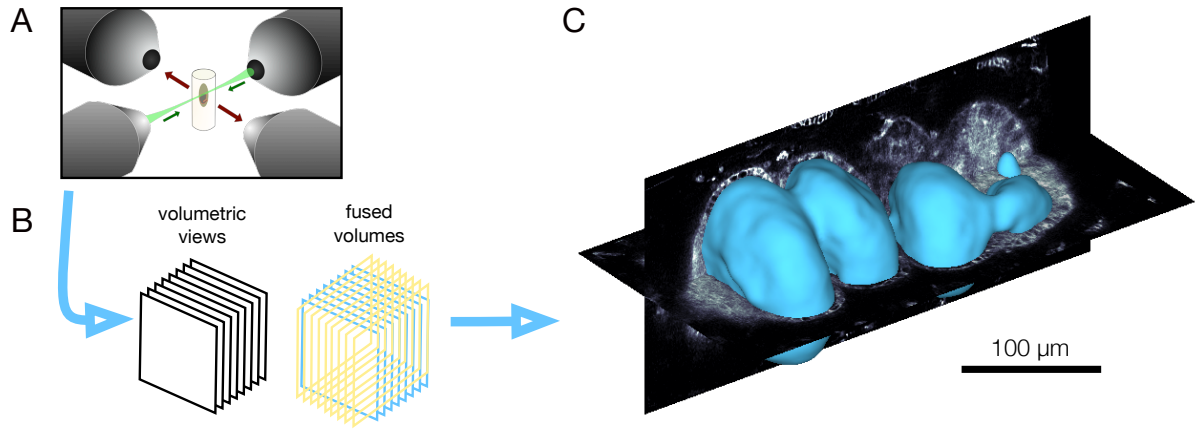

Figure 1 - supplement 1: **Multi-view light sheet microscopy enables volumetric imaging.** *(A)* We illuminate embryos embedded in an agarose column via a laser beam emerging from two illumination objectives (green). The laser sweeps along the long axis of the column to raster a sheet of light. Two detection objectives capture fluorescence in the orthogonal axis (red arrows). *(B)* By translating, rotating, and repeating, we build volumetric views from a series of angles. *(C)* Through fusion and deconvolution, multiple volumetric views build data volumes with nearly isotropic resolution for analysis.

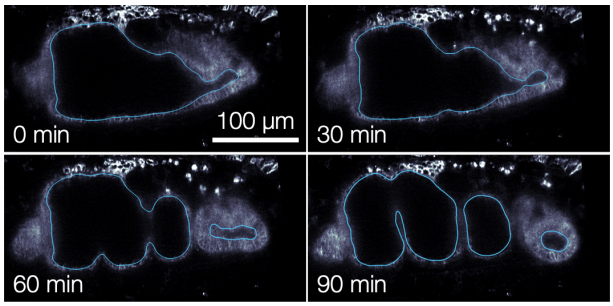

Figure 1 - supplement 2: **Organ segmentation via morphological snakes level sets.** Automatic segmentation of the apical (inner) surface of the endoderm minimizes a non-local Chan-Vese energy functional [31, 30] to encapsulate yolk without enclosing midgut tissue, shown for four snapshots of mid-sagittal sections using TubULAR [32]. Blue contours mark the surface intersection with the mid-sagittal plane.

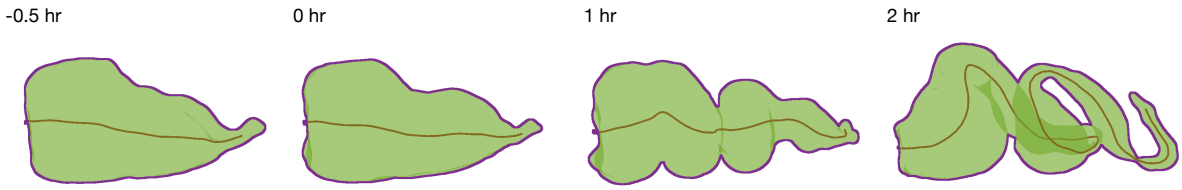

Figure 1 - supplement 3: **A centerline measures an effective length of the organ.** We compute the centerline (brown curve) using the TubULAR package for extracted shapes (green with purple boundary for clarity). The cumulative length of these curves defines the effective length of the organ reported in Fig. 1.

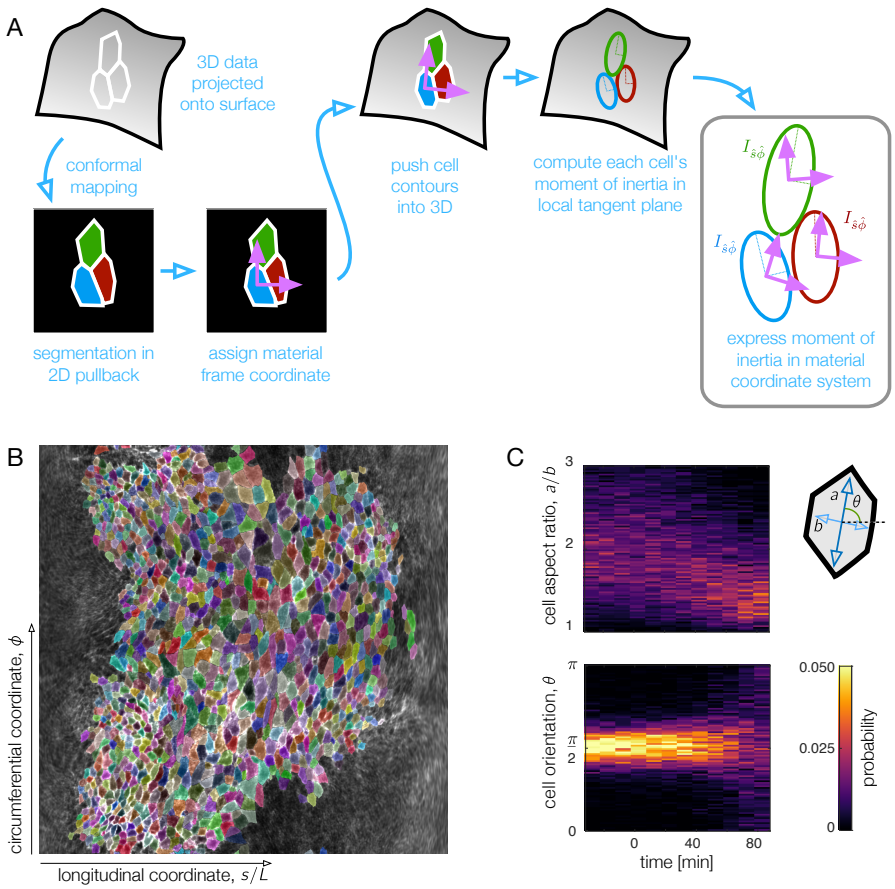

Figure 2 - supplement 1: **Surface projection aids in quantifying cell shape change in the 3D tissue surface.** *(A)* To measure cell shapes, we trace cell membrane contours in a conformal mapping to a 2D pullback plane and re-embed cells into local tangent planes in 3D for shape quantification. After surface extraction, we project the data on a midgut surface $\sim$2.5 μm beyond the apical side of the endoderm to the plane for segmentation. The pullback plane also defines material coordinate directions in which we can measure orientation of cells, θ. By projecting cell contours back into 3D, we compute moment of inertia tensors for each cell in a local tangent plane. The eigenvalues and eigenvectors of the moment of inertia tensors define the cell anisotropy a/b and the orientation of their long axis, θ, with respect to material coordinate directions $\hat{s}$ and $\hat{\phi}$. *(B)* Example segmentation in the pullback plane at a time near the onset of the first constriction. Each cell polygon is given a random, distinguishable color to demonstrate the segmentation quality. *(C)* Here shown in raw histograms, cell aspect ratios decrease and condense close to 1 (isotropic shapes) by $\sim$80 minutes after the onset of the first (middle) constriction. During this time, the cells do not rotate, as evidenced by the sustained peak in cell orientation near zero. At late times, when the cells are nearly isotropic, the orientation becomes less clearly defined and the distribution broadens.

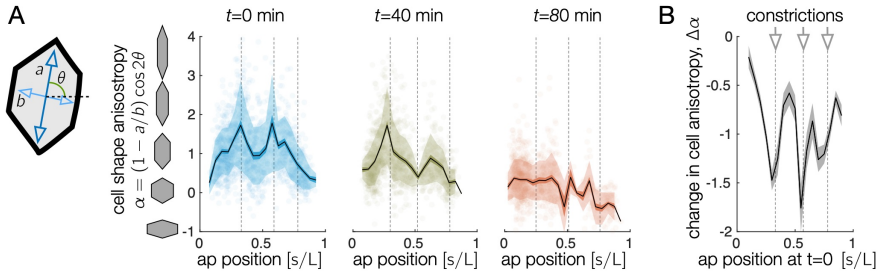

Figure 2 - supplement 2: **Endodermal cells are initially most elongated near anterior and middle constrictions, and cell shape change is greatest near constrictions.** *(A)* The oriented cell anisotropy varies along the anterior-posterior axis. We define the cell shape anisotropy to be a signed quantity varying from positive for cells elongated along the circumferential axis and negative for cells elongated along the longitudinal axis. This signed measure of oriented anisotropy shows that some cells become elongated along the longitudinal (AP) axis, particularly near the posterior end of the midgut by $t = 80$ min. In particular, the signed shape anisotropy of a cell is $\alpha \equiv (1 - a/b)\cos 2\theta$, where a and b are the semimajor and semiminor axes of the ellipse capturing each cell's moment of inertia tensor and θ is the cell's angle with respect to the material frame's longitudinal axis. Locations of the constrictions or constriction precursors are marked in dashed gray vertical lines. Cells near the anterior and middle constrictions are initially elongated along the circumferential axis more than cells in the interstitial regions. Cell anisotropy changes dramatically first at the middle constriction, then at the anterior and posterior constrictions. Shaded error bars denote standard deviations (semi-transparent bands) and standard error on the mean (opaque colored bands), while black curves denote the mean. *(B)* The total change in signed cell shape anisotropy over the 80 minute timecourse shows strong, negative values near each constriction. We here parameterize cells' anterior-posterior positions at $t = 80$ by mapping to their locations at $t = 0$ in order to compare measurements made in the same tissue patches.

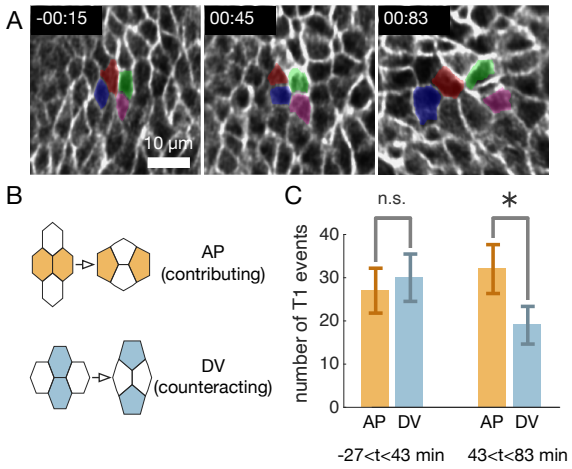

Figure 2 - supplement 3: **Topological rearrangements occur in the endoderm but are not aligned during the earliest stages of gut constrictions, consistent with cell shape change being the dominant contributor to tissue deformation at the onset of constrictions.** *(A)* An example rosette of four tracked cells. The tissue patch is flattened to a plane such that the longitudinal and circumferential axes of the organ in the material frame aligns with the horizontal and vertical axis, respectively. The mapping to the plane is an as-rigid-as-possible map constrained so that the ratio of lengths in the longitudinal and circumferential directions is preserved near the center of the image (so the diagonal metric tensor components are equal $g_{11} \approx g_{22}$). *(B)* Here we define T1 events to be AP oriented if the cells that lose contact are within 45° of the longitudinal axis of the organ in the material frame. Conversely, in DV oriented T1 events, the cells that lose contact are within 45° of the circumferential axis of the organ in the material frame. *(C)* In a collection of 175 tracked cells in the anterior midgut, we find no significant difference between the rate of cell intercalations oriented along the longitudinal direction versus the circumferential direction during stages 15-16a of constrictions ($-27 < t < 43$ min), while we find a bias in T1 orientations during later stages of 16a and 16b ($43 < t < 83$ minutes) among the tracked cells. Uncertainties are taken as the square root of the count, and $* = p < 0.05$

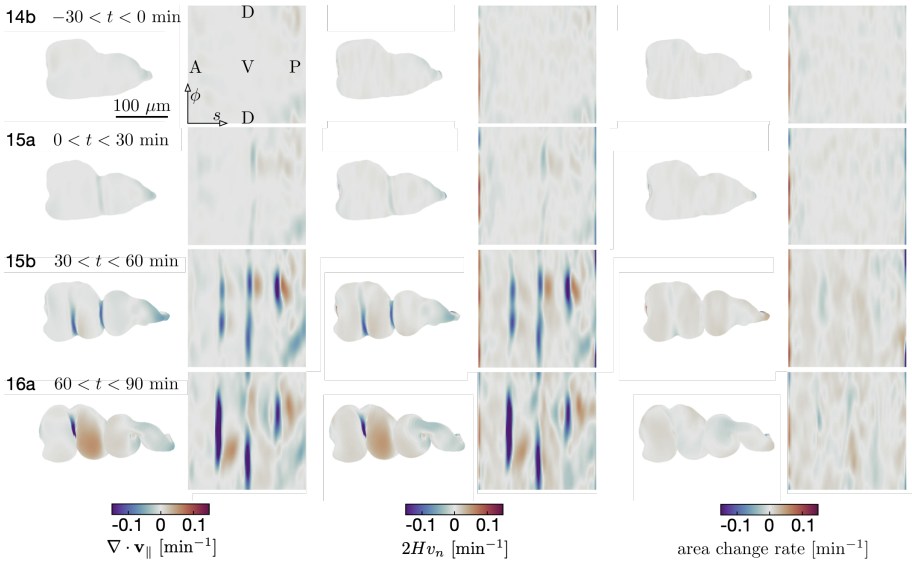

Figure 3 - supplement 1: **Dilatational flow patterns are tightly coupled to bending throughout midgut constrictions, indicating a nearly incompressible tissue behavior.** Resulting divergence of in-plane tissue motion ($\nabla \cdot \mathbf{v}_{\|}$) and out-of-plane deformation measurements ($2Hv_n$) on an representative embryo, plotted both on the midgut surface in 3D and in pullback coordinates, show strong correlation. The difference of the two patterns gives the local area change (right columns). Each image is the average of patterns over a 30 minute timespan, while Video 5 shows the instantaneous measurements. The pullback representation uses the surface Lagrangian parameterization (s, ϕ), such that the ventral tissue is in the midline of the image, anterior is to the left, posterior is to the right, and deformation of the organ shape in 3D is subtracted out from the pullback coordinates of subsequent timepoints [32]. The s position in the pullback representation is proportional to the proper distance along the organ's longitudinal axis.

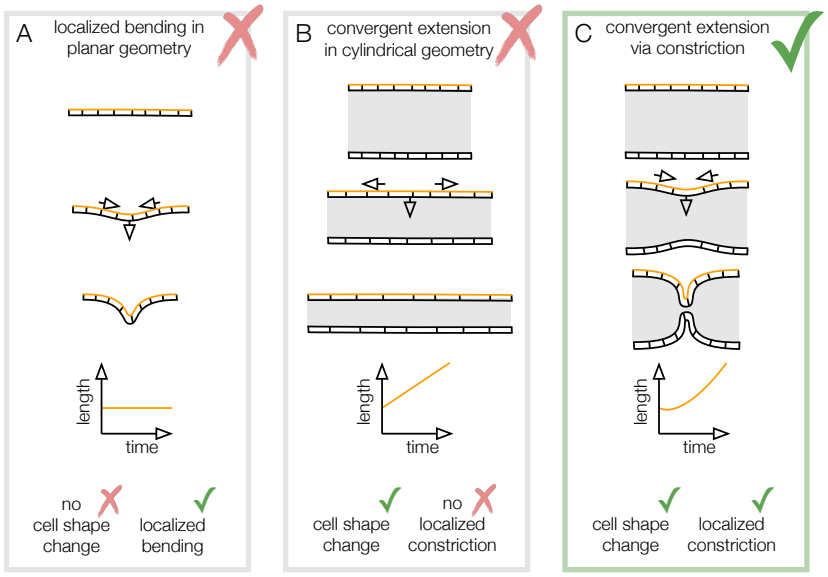

Figure 3 - supplement 2: **Convergent extension via constriction links in-plane tissue shape change with out-of-plane deformation.** *(A)* An initially flat, incompressible sheet may bend in a localized region without deforming the tissue in-plane. Distances between cells in plane are preserved, illustrated by the constant length between the ends of the sheet along the orange geodesic. *(B)* A uniformly constricting, incompressible tube exhibits convergent extension but has no localized folds. In the absence of cell intercalations, cells converge along the circumferential direction and elongate along the longitudinal direction, so an orange curve spanning several cells along the longitudinal axis lengthens over time. *(C)* In convergent extension via constriction, localized normal motion of the tube couples to in-plane tissue shape change. In a constricting, incompressible tube, the tissue converges along the circumference and extends along the bending longitudinal profile.

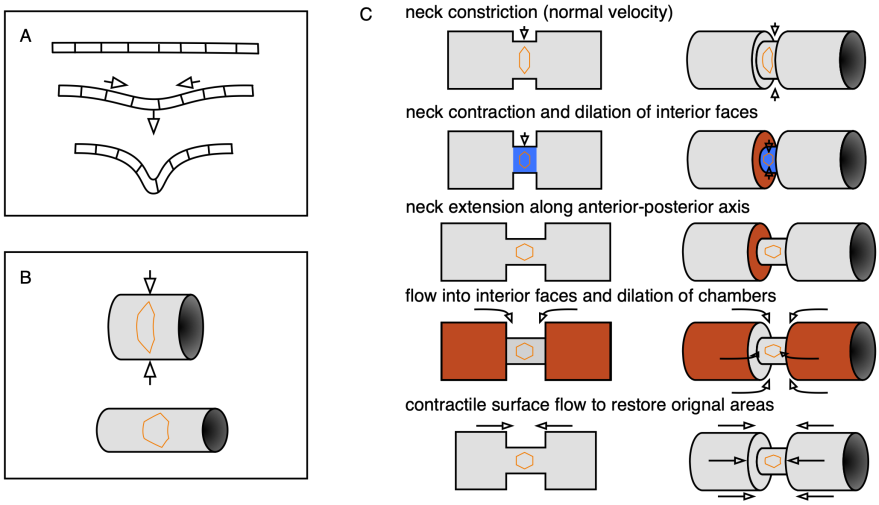

Figure 3 - supplement 3: **Three-component decomposition of kinematics elucidates coupling between compressibility and convergent extension.** *(A)* An initially flat incompressible sheet demonstrates kinematic coupling between in-plane dilatational flow and out-of-plane bending to preserve cells' 2D areas. *(B)* Constriction couples to convergent extension via curvature of the surface. As a tube constricts, the tube elongates in order to preserve surface area. Correspondingly, cells change their aspect ratio and undergo convergent extension. *(C)* The two effects shown in (A) and (B) couple in a pinching tube with a localized constriction. A tube with a step-like constriction is composed of deformable cells whose areas shall not change. Constriction of the narrow tube via inward normal velocities would decrease the neck area (blue), so the neck extends to keep its area fixed. This is convergent extension. The faces are now dilated, triggering flow into the interior faces to correct for the change in tissue density. In this way, convergent extension is linked to incompressibility, which couples in-plane dilatational flow to out-of-plane deformation.

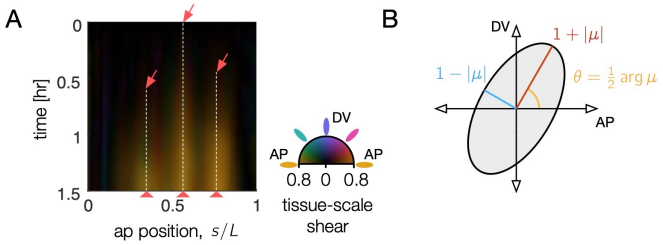

Figure 3 - supplement 4: **Tissue shear generates 3D convergent extension during constrictions, as captured in the Beltrami coefficient – a local measure of anisotropic, area-preserving deformation.** *(A)* Tissue-scale shear accumulates near each constriction, shown as a kymograph in the material coordinate frame averaged along the circumferential axis. As time increases (downward), orange streaks reflect area-preserving convergence of tissue patches along the organ circumference and extension along the folding AP axis near constrictions (red arrows). Here, the organ is parameterized by the position, s, at the onset of constriction ($t = 0$), measured in proper length along the surface, and deformation is averaged along the circumferential position in the kymograph. Color denotes the orientation of the anisotropic shear deformation in this material frame, such that shear which converges along the circumferential axis and extends along the AP axis is denoted by orange color (colorwheel). Larger magnitudes of tissue shear are brighter, reflecting the Beltrami coefficient averaged over the circumferential axis. *(B)* The Beltrami coefficient μ is defined as the amount of area-preserving shear transforming a circle into an ellipse with aspect ratio $1 + |\mu|/(1 - |\mu|)$ at an angle $\arg \mu/2$.

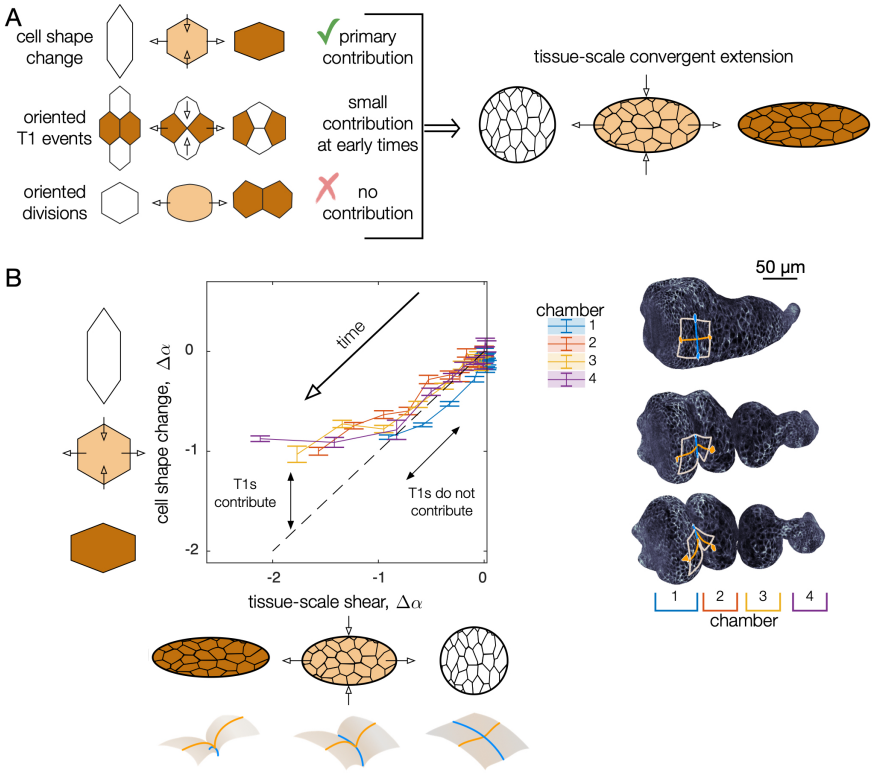

Figure 3 - supplement 5: **Cell shape change quantitatively accounts for tissue-scale convergent extension during early stages of midgut constrictions.** *(A)* As constrictions form, cells change shape from elongated circumferentially to elongated along the longitudinal axis of the organ. At the same time, the tissue deformation mirrors the cell shape change, converging along the circumference and elongating along the longitudinal axis of the organ. Cell intercalations (T1 events) could also contribute to convergent extension if oriented. We find these make a small contribution at early stages of constriction and a large contribution at later stages. No signs of divisions are present, so we rule out oriented cell divisions as contributors to convergent extension. *(B)* Tissue-scale deformation quantitatively tracks cell shape change at early times, while intercalations contribute to convergent extension at later stages. Change in cell shape anisotropy (assessed over all cells in each chamber) is plotted against the magnitude of tissue convergent extension (averaged over the same tissue positions in each chamber). On the vertical axis, we report cell shape change as the average cell shape anisotropy for all segmented cells in each chamber $\langle\alpha(t)\rangle$, minus the mean value for each chamber at the onset of the middle constriction $\langle\alpha(t=0)\rangle$, such that $\Delta\alpha(t) \equiv \alpha(t) - \langle\alpha(t=0)\rangle$. Given that cells' orientations are steady during constrictions, we use a scalar measure of oriented cell shape anisotropy, $\alpha = (1 - a/b)\cos 2\theta$, where a and b are the semimajor and semiminor axes of the ellipse capturing each cell's in-plane moment of inertia tensor and θ is the cell's angle with respect to the material frame's longitudinal axis. To compute a tissue-scale shape change for comparison, we advect the cell contours of the initial segmentation along the meso-scale tissue flow and compute the cell shape anisotropy of the advected segmentation [32]. Chambers are numbered from anterior (1) to posterior (4), separated by constriction locations. Tick marks denote standard errors on the mean for cell anisotropies within each chamber.

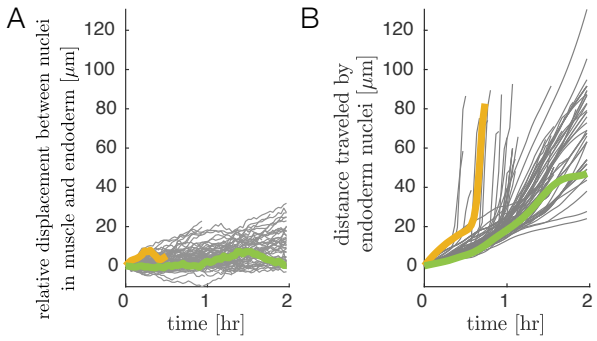

Figure 4 - supplement 1: **Relative motion of endodermal and mesodermal nuclei is small compared to motion of the tissue.** *(A)* Tracking muscle nuclei and counterpart nuclei in the endoderm reveals only a gradual increase in geodesic distance (distance along the gut surface) between initially close nuclei pairs over time. The mean displacement grows by $\sim$5 μm per hour during folding on average, regardless of whether nuclei are located in deep folds (as in the example pair marked by a yellow curve) or on the surface of the gut chambers (green curve). *(B)* In contrast, the tissue deformation leads to large displacements of cells. We measure distances in embedding space along pathline trajectories suitably smoothed to remove contributions from noise and transient motions. Distance traveled for example tracks invaginating into deep folds (yellow curve) or translating on gut chambers (green curve) are highlighted to match panel (A).

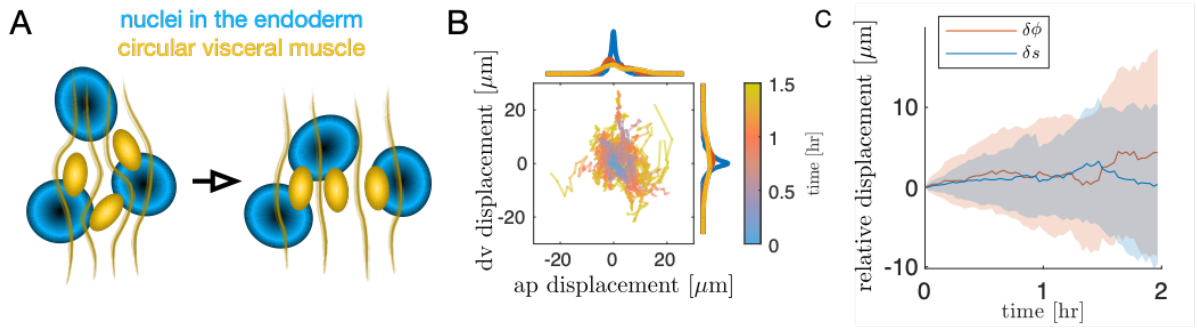

Figure 4 - supplement 2: **Motion of the muscle nuclei with respect to the endoderm is not coherent.** *(A)* Schematic of muscle nuclei configuration at early and late times. Muscle cells are positioned in bands along the AP axis and are initially clustered, such that each band is several cells wide along the circumferential axis. As constrictions form, circumferential muscle nuclei arrange in a nearly single-file configuration. *(B)* Motion of nuclei cells relative to the endodermal layer does not show strongly coherent (directional) motion, as demonstrated by individual tracks of relative displacement colored by timestamp. As before, the positions of 81 nuclei cells are measured relative to the center of mass of the endodermal nucleus that was nearest at the onset of constrictions. Distances are measured as geodesic lengths along the surface. Distances along the normal direction (through the thickness of the tissue) are ignored. That is, nuclear positions are projected along the thickness of the tissue onto the surface in which the endodermal nuclei reside. Histograms of accumulated displacements in either direction show the average over the first 30 minutes (blue), 30-60 minutes (red), and 60-90 minutes (yellow). *(C)* The same data shown in (B) is plotted as a distribution, with each component separated. The standard deviation of displacement coordinates (colored bands), either in the $\hat{s}$ direction (along the folding longitudinal axis in the material frame, blue) or the $\hat{\phi}$ direction (along the circumferential axis in the material frame, orange) show an increase of $\sim$5 μm per hour, with nearly zero mean displacement in either axis.

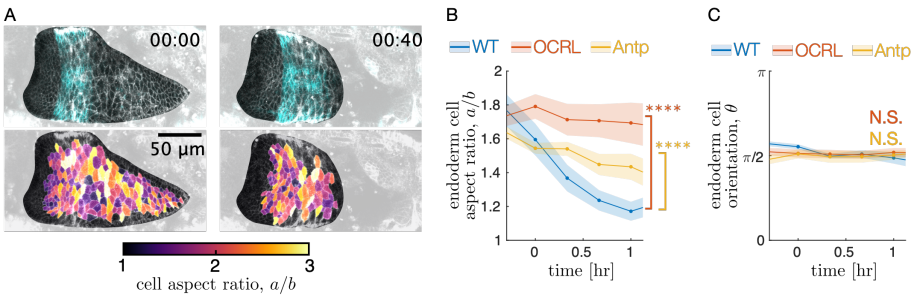

Figure 4 - supplement 3: **Optogenetic knockdown of muscle contractility inhibits endodermal shape changes, mimicking mutant behavior.** *(A)* Snapshots of single-cell shape measurements of embryos under optogenetic perturbations demonstrate that muscle contraction induces endoderm cell shape change. During optogenetic inhibition of muscle contractility in the *Antp* domain using *w,Antp-GAL4× w; UAS-CIBN::pmGFP;UAS-CRY2-OCRL*, cell shapes in the interior two chambers (which remain as a single chamber in the optogenetic mutant) remain steady. *(B)* Endodermal cells undergo less shape change in both *CRY2-OCRL* and *Antp* mutants, as reported in the main text. As before, $****$ denotes $p < 0.0001$, and N.S. denotes $p > 0.05$. *(C)* The endodermal cell orientation does not change significantly between conditions.

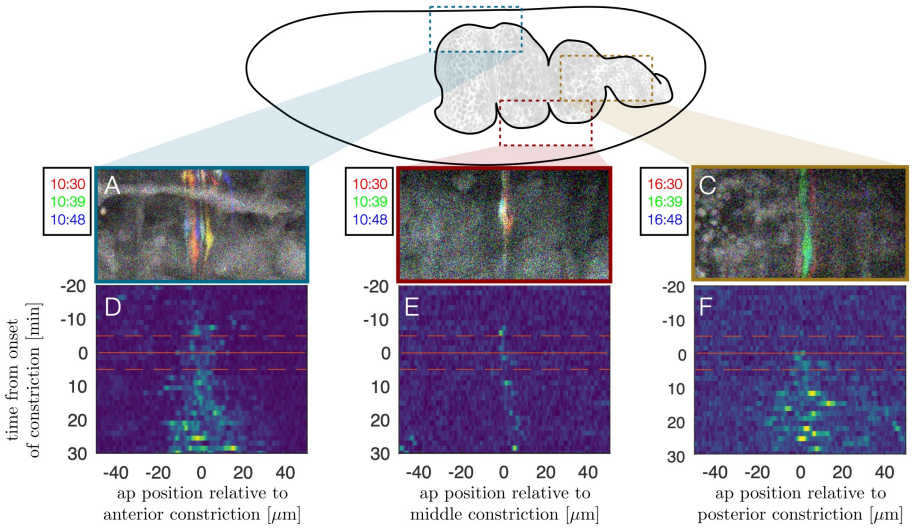

Figure 5 - supplement 1: **Kymographs of *GCaMP6s* dynamics show that calcium activity is initially localized in space to constrictions and begins near the time at which constrictions begin.** For each constriction, the transient signal is computed (colored signals in snapshots A-C) and averaged across the DV direction (in the lab frame) into a space-time heatmap (D-F). A time of $t = 0$ min for each panel corresponds to the time when localized constriction is visible in the bright-field channel at that constriction location and carries an uncertainty of ± 5 minutes (dashed orange lines). The middle constriction (the sharpest fold, B and E) has the sharpest activity profile, and the posterior constriction (the widest fold, C and F) has the broadest activity profile.

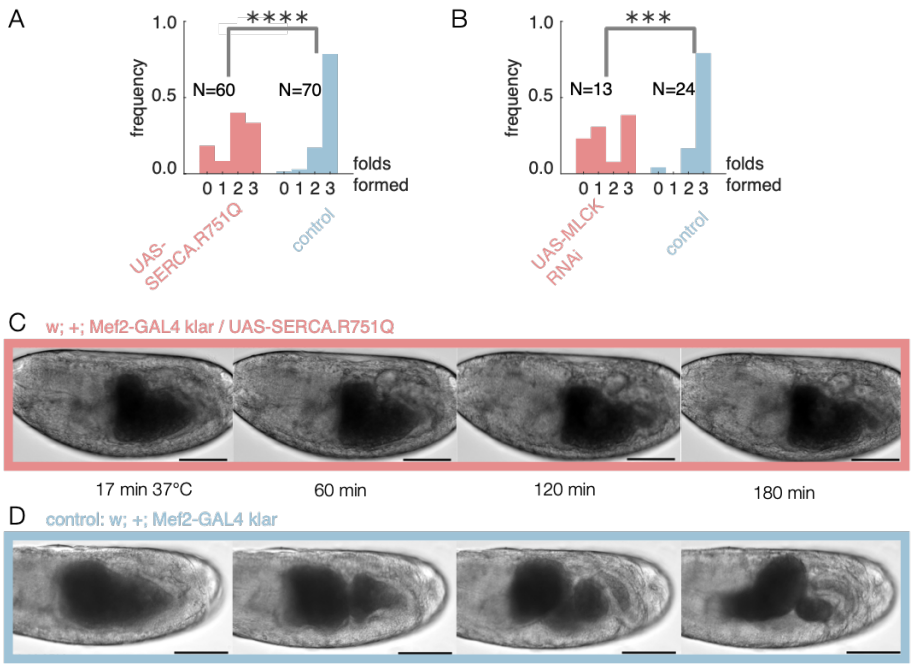

Figure 5 - supplement 2: **Disrupting calcium activity hinders constrictions.** *(A)* Embryos expressing a dominant negative form of SERCA have fewer successful constrictions on average (single tailed Z-test, $N = 130$, $p = 3 \times 10^{-8}$) using a muscle-specific driver, *Mef2-GAL4*, at elevated temperatures (continuous heatshock at 37°C). In adult flies, this dominant negative SERCA was previously shown to exhibit temperature-sensitive expression and inhibits muscle contractions at 37°C [46]. *(B)* Embryos expressing RNAi against MLCK have fewer successful folds on average (single tailed Z-test, $N = 37$, $p = 0.002$). Here we use a ubiquitous driver, *tub15-GAL4; tub67-GAL4* under continuous heatshock starting during or just after midgut closure, before constrictions appear. *(C)* Brightfield imaging of embryos expressing a mutant form of *SERCA* in muscles show reduced folding activity. Here, driving a mutant *SERCA* expression via heatshock starting at stage 15a shows no folds. *(D)* Control embryos without the mutant form of *SERCA*, in contrast, typically form three folds. Timestamps denote minutes since the onset of heatshock and scalebar is 100 μm.

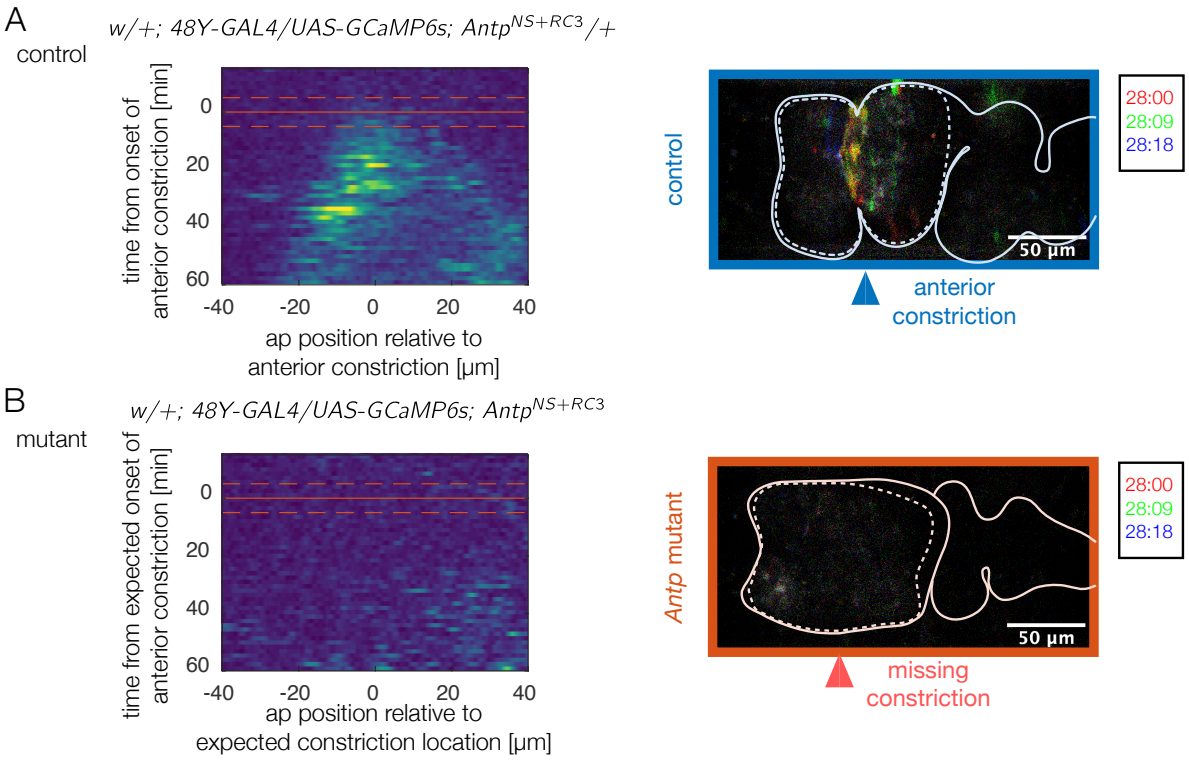

Figure 5 - supplement 3: ***Antp* mutants show reduced calcium activity in the anterior two chambers for over an hour.** *(A)* Kymographs of wild-type calcium dynamics near the anterior fold for $N = 13$ control embryos show fluctuating calcium activity beginning at the onset of folding at the site of the fold. The domain of calcium activity broadens anteriorly and posteriorly in time. A red solid line marks the onset of the anterior constriction, and dashed lines denote the precision with which this time is known. *(B)* In mutants, almost no calcium pulses are observed during the same timespan. A kymograph of average fluctuating *GCaMP6s* intensity for $N = 5$ *Antp* mutants remains quiescent (dark blue). Given that the anterior fold does not form, $t = 0$ was prescribed based on the depth of the posterior fold. The expected position of the anterior fold (which defines the horizontal axis of the kymograph) is inferred from the position of the anterior fold relative to the anterior face of the midgut in control embryos.

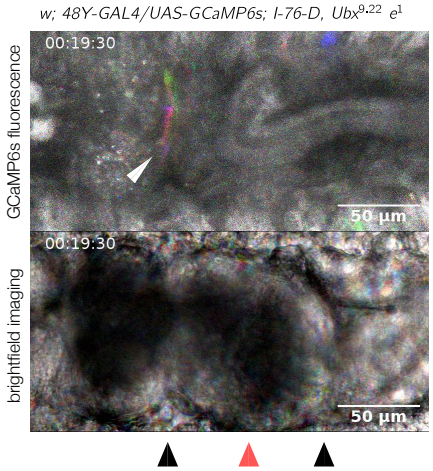

Figure 5 - supplement 4: **Calcium pulses appear at the unaffected anterior constriction in *Ubx* mutants.** A dorsal view snapshot of pulsing calcium activity (top panel) and the associated brightfield image (bottom panel) of a *Ubx* mutant shows calcium pulses in the anterior constriction (white arrowhead). Each image is an overlay of maximum intensity projections for three shallow confocal stacks taken 10 seconds apart and false-colored red, green, and blue for each respective stack. The colorful streak near the anterior constriction reflects the transient pulses at that location. As in Fig. 5F and Fig. 5 - supplement 3, the posterior constriction lies outside the confocal stack and is therefore not visible in the *GCaMP6s* channel. This data suggest the calcium dynamics at each constriction are regulated locally along the length of the midgut ($N = 5$).